JGR Solid Earth

RESEARCH ARTICLE
10.1029/2020JB020052

Key Points:
- We present the first probabilistic model of interseismic aseismic slip throughout seismogenic depth along 100 km of the Philippine Fault
- Joint inversion for anthropogenic subsidence and fault deformation reveals downdip locking from the surface on a 20-km section in Tongonan
- Extent of seismic rupture of the July 2017 magnitude 6.5 and 5.8 earthquakes correlates with geometric complexity and lack of slip deficit

Supporting Information:
- Supporting Information S1

Correspondence to:
J. D. B. Dianala,
john.dianala@earth.ox.ac.uk;
jddianala@nigs.upd.edu.ph

Citation:
Dianala, J. D. B., Jolivet, R., Thomas, M. Y., Fukushima, Y., Parsons, B., & Walker, R. (2020). The relationship between seismic and aseismic slip on the Philippine Fault on Leyte Island: Bayesian modeling of fault slip and geothermal subsidence. *Journal of Geophysical Research: Solid Earth*, *125*, e2020JB020052. https://doi.org/10.1029/2020JB020052

Received 23 APR 2020
Accepted 20 OCT 2020
Accepted article online 24 OCT 2020

The Relationship Between Seismic and Aseismic Slip on the Philippine Fault on Leyte Island: Bayesian Modeling of Fault Slip and Geothermal Subsidence

John Dale B. Dianala[1,2], **Romain Jolivet**[3,4], **Marion Y. Thomas**[5], **Yo Fukushima**[6], **Barry Parsons**[1], and **Richard Walker**[1]

[1]COMET, Department of Earth Sciences, University of Oxford, Oxford, UK, [2]National Institute of Geological Sciences, University of the Philippines Diliman, Quezon City, Philippines, [3]Laboratoire de Géologie, Département de Géosciences, École Normale Supérieure, PSL Université, UMR 8538, Paris, France, [4]Institut Universitaire de France, Paris, France, [5]Sorbonne Université, CNRS-INSU, Institut des Sciences de la Terre Paris, ISTeP UMR 7193, Paris, France, [6]International Research Institute of Disaster Science, Tohoku University, Sendai, Japan

Abstract

Delineating seismic and aseismic slip on faults allows the exploration of the complex relationship between these different modes of slip. Further, quantifying them helps in the assessment of seismogenic potential. We present a distributed slip model of the rate of aseismic slip along the Leyte island section of the Philippine Fault and make comparisons with the extent of seismic slip from the latest significant earthquakes in July 2017. We derived both coseismic and aseismic slip distributions from kinematic inversions of synthetic aperture radar interferometric (InSAR) observations using a probabilistic (Bayesian) framework. Velocity maps from stacking and time series analysis of ALOS interferograms spanning 4 years (2007–2011) show a step change in ground deformation right on the fault. Inverting for slip at depth reveals along-strike variations of aseismic slip rate over ∼100 km. Aseismic slip on the surface reaches rates of more than 3 cm/yr, equivalent to the long-term slip rate (3.3 ± 0.2 cm/yr). Over the same period, a 20-km segment in Tongonan appears to be locked. This segment ruptured in M_w 6.5 and M_w 5.8 earthquakes on 6 and 10 July 2017, respectively, as constrained by Sentinel-1 and ALOS-2 InSAR data. Seismic slip appears to be restricted within the Tongonan segment, with up to 152 ± 21 cm of left-lateral displacement. The slip budget and complementarity between the extents of interseismic and coseismic slip suggest that a seismogenic asperity exists in Tongonan. The presence of active hydrothermal systems and rate-strengthening materials provide physical conditions that can promote aseismic slip.

Plain Language Summary

In July 2017, the Philippine Fault on Leyte island produced a damaging earthquake that was unexpected. Previous studies that tracked the movement of the Earth's crust have suggested that the fault in Leyte does not accumulate strain, and hence stress, as the fault primarily slides stably and slowly. This is in contrast to earthquake-generating faults that go on a cycle of building up stress for a long period of time, due to the crust staying stuck (or locked) on the fault, and then releasing the stored stress as an earthquake. With analysis of high-resolution satellite radar, we now show that while 100 km of the fault indeed appears to be moving slowly and gradually, a 20-km-long portion in the middle of the fault appears to be locked. Our observations and models of the July 2017 earthquake confirm that this same section of the fault alone moved then. The geometry of the fault, the abundance of fluids, and the presence of specific types of minerals may all play a role on how the fault behaves. This work is the first of its kind on the Philippine Fault, highlighting the importance of exploring relatively less well studied faults and their physical properties.

1. Introduction

Faults that slip aseismically, as opposed to locked faults, are often considered less likely to generate large earthquakes due to the lack of long-term strain accumulation. Hence, the seismogenic potential of faults can be assessed by appraising the degree and extent of locking on faults and by exploring the relationship between seismic and aseismic slip (Avouac, 2015; Harris, 2017). Geodetic and seismological observations show that fault segments that appear to slip aseismically on the surface may host locked sections at depth. This has been made apparent on relatively well studied faults in California (USA) (e.g., Burgmann et al., 2000; Chaussard et al., 2015; Jolivet, Simons, et al., 2015; Johnson, 2013; Lienkaemper et al., 2012; Tse et al., 1985), most strikingly along the central section of the San Andreas Fault, where the Parkfield segment has hosted repeated strong earthquakes on a locked asperity (e.g., Bakun et al., 2005). Continental faults in other settings, including the Longitudinal Valley Fault (Taiwan) and the Alto Tiberina Fault (Italy), also show a similar behavior of partial locking with a potential for strong earthquakes (e.g., Anderlini et al., 2016, and Thomas, Avouac, Champenois, et al., 2014, respectively). In addition, numerical models based on rate-and-state friction suggest that seismic ruptures may propagate across sections of faults that host aseismic slip during the interseismic period (e.g., Noda & Lapusta, 2013; Thomas et al., 2017). Isolating seismogenic asperities and documenting how far seismic slip propagates into sections that slip aseismically is therefore key in estimating seismic hazard, especially when these faults run across populated regions.

Many advances in understanding the diverse spatial and temporal nature of aseismic slip on continental faults have been brought about by interferometric synthetic aperture radar (InSAR) (Bürgmann, 2018; Jolivet & Frank, 2020). Thanks to its fine resolution, global coverage, and convenient access to the data, space geodesy using InSAR has become a powerful tool for studying earthquakes and active tectonics (Elliott et al., 2016). The earliest InSAR observations of the seismic cycle revolutionized our ability to explore fault and crustal mechanics (e.g., Deng, 1998; Massonnet et al., 1993; Peltzer et al., 2001; Price & Sandwell, 1998; Wright et al., 2001). Continuous monitoring through interseismic periods has further enabled us to delineate aseismic slip on remote and less well instrumented faults (e.g., Cavalié et al., 2008; Cetin et al., 2014; Jolivet et al., 2013; Fattahi & Amelung, 2016; Pousse Beltran et al., 2016; Thomas, Avouac, Champenois, et al., 2014; Tong et al., 2018). This allows us to discover and explore potential earthquake sources that might not be well known, like on faults sometimes referred to as "creeping faults" (e.g., Jolivet, Simons, et al., 2015).

For two decades, shallow aseismic slip of more than 2.0 cm/yr on the Leyte island section of the Philippine Fault has been measured using sparse GPS surveys alone (Duquesnoy et al., 1994; Duquesnoy, 1997) (Figure 1). The similarity of these estimates to the long-term slip rate, along with the lack of induced seismicity from injection experiments, has led to the notion that this portion of the fault is primarily aseismic (Prioul et al., 2000). However, on 6 July 2017, a moment magnitude (M_w) 6.5 earthquake occurred in Leyte (Fukushima et al., 2019; PHIVOLCS, 2017; Yang et al., 2018). With up to 1.1 m of slip on the surface, most prominently in the village of Tongonan, within the city of Ormoc, the M_w 6.5 earthquake registered Intensity VIII shaking (on the PHIVOLCS Earthquake Intensity Scale) near the epicenter (Llamas et al., 2017; PHIVOLCS, 2017). The temblor happened in populated areas, resulting to three deaths and widespread economic disruption (PHIVOLCS, 2017). InSAR has been used to model the extent of seismic slip (Yang et al., 2018) and to juxtapose the seismogenic section with the surface manifestation of aseismic slip in the interseismic (Fukushima et al., 2019). However, anthropogenic subsidence adjacent to the fault and the coeseismic area has hindered detailed comparisons of interseismic and coseismic slip distribution (Fukushima et al., 2019). Furthermore, abundant geothermal resources in Leyte have spurred more than 30 years of detailed geological investigations on and near the fault, even up to around 2 km depth (e.g., Caranto & Jara, 2015; Reyes, 1990; Scott, 2001), allowing the rare opportunity to directly correlate in-situ physical conditions of an active fault with its behavior.

In this study, we constrain interseismic deformation from fault and anthropogenic subsidence sources in Leyte and analyze the relationship between aseismic and seismic slip modes. The distributed slip models that we present are the first of their kind on the Philippine Fault, as we invert for the subsidence parameters and slip rates through probabilistic (Bayesian) approaches. This permits us to explore how fault zone geometry and geological conditions correlate and might control the distribution of the slip modes, adding to a rich body of literature on fault and earthquake mechanics. Independent of the available InSAR data, we incorporate information from leveling surveys (from Apuada et al., 2005) to understand the anthropogenic subsidence source. For coseismic displacements, we isolate the slip of the July 2017 mainshock from that of a M_w 5.8 aftershock, which are combined in previous coseismic slip models (Fukushima et al., 2019; Yang et al., 2018), and this shows how the spatiotemporal distribution of seismic slip might relate to geometrical complexity of the fault. Finally, we provide a physics-based framework for estimating the earthquake return time in a probabilistic sense and check this against the possibility of the July 2017 earthquake as a repeat of a surface magnitude (M_s) 6.9 event in 1947 (Fukushima et al., 2019), which is of societal importance.

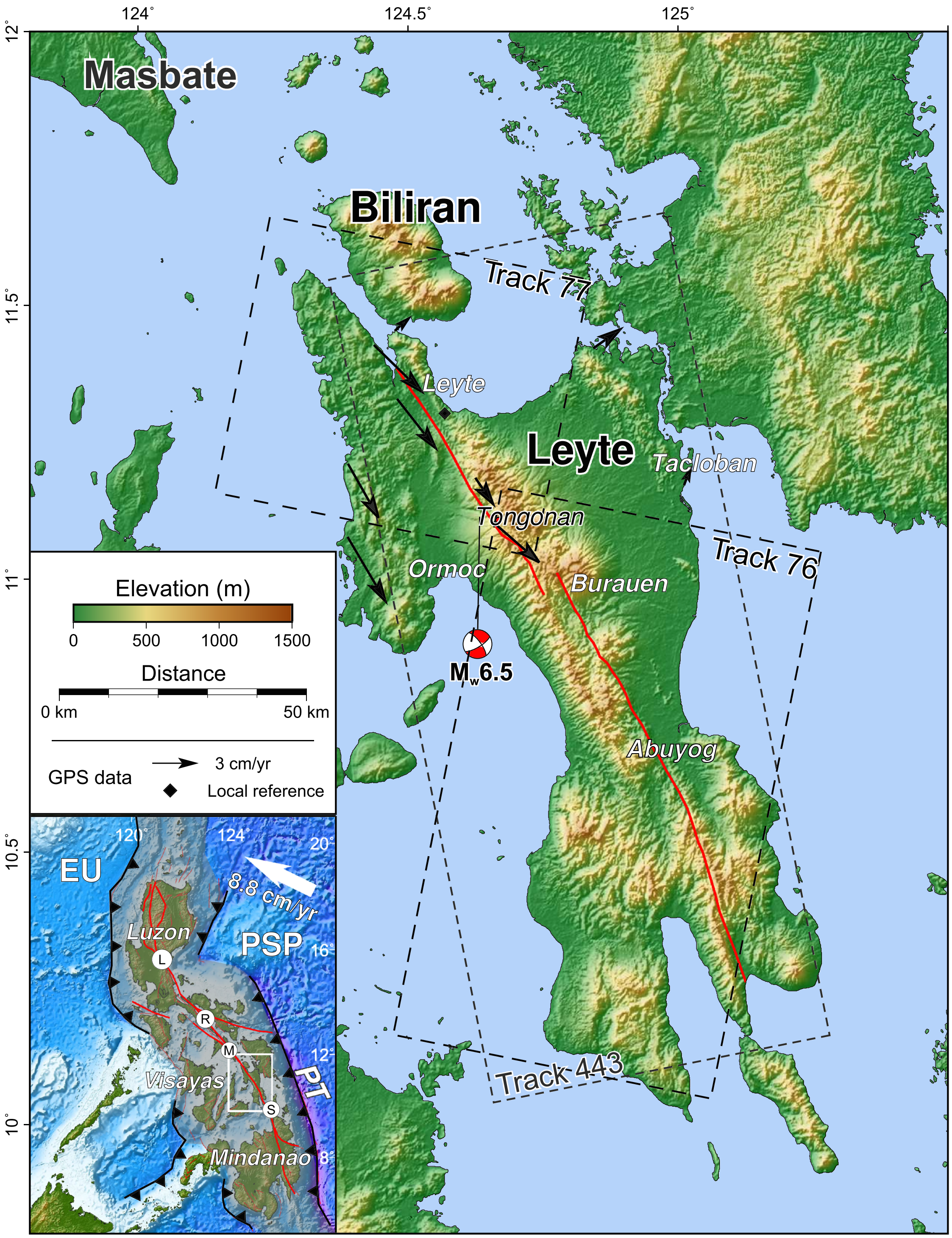

Figure 1. Active tectonics of the island of Leyte in the Philippines. Shaded relief map is based on SRTM 30-m resolution elevation data. Surface trace of the Philippine Fault (red, modified from Tsutsumi & Perez, 2013) is based on observations from AirSAR-derived DEM and InSAR. Arrows are GPS-derived velocities from Duquesnoy (1997) relative to a local reference station (black diamond). Red "beach ball" indicates the mechanism of the 6 July 2017 M_w 6.5 earthquake (USGS). Long and short black dashed lines indicate spatial coverage of ALOS data in ascending (Track 443) and descending (Tracks 76 and 77) passes, respectively. Inset: Geographic location of Leyte (white box) with respect to regional tectonic features around the Philippine Mobile Belt (shaded area) (modified from Aurelio et al., 2013). White circles = epicenters of known historical and recent surface-rupturing earthquakes (see text for discussion): L = Luzon, magnitude M_w 7.7, 1990; R = Ragay Gulf, M_s 7.3, 1973; M = Masbate, M_s 6.2, 2003; S = Surigao, M_s 6.9,1879 and M_w 6.5, 2017. White arrow indicates the velocity of the Philippine Sea Plate (PSP) relative to the Eurasian Plate (EU) (DeMets et al., 2010). Sawtooth pattern: subduction zones, with PT denoting the Philippine Trench.

2. Tectonic Setting

2.1. The Philippine Fault: Geodynamic and Seismic Context

The Philippine Fault is an approximately 1,200-km-long left-lateral strike-slip fault (Allen, 1962; Tsutsumi & Perez, 2013). It accommodates part of the the oblique convergence between the Philippine Sea Plate and the Philippine Mobile Belt, on the margin of the Eurasian Plate, in a strain partitioning regime (Aurelio, 2000; Barrier et al., 1991) (Figure 1). The Philippine Sea Plate moves northwestward at around 8.8 cm/yr relative to a fixed Eurasian Plate (DeMets et al., 2010). Regional Euler pole rotation suggests that the Philippine Fault has a long-term strike-slip rate of 1.9–2.5 cm/yr (Barrier et al., 1991). In the northern Philippines, 100–150 km-long GPS transects indicate a long-term slip rate of 2.4–4.0 cm/yr on the Philippine Fault (Galgana et al., 2007; Yu et al., 2013). These estimates, however, go across several branches of the fault on Luzon island. More detailed block models from campaign surveys suggest interseismic slip rates of around 0.7 to 3.1 cm/yr on individual branches of the Philippine Fault in Luzon (Hsu et al., 2016).

Geologic, geodetic, and seismotectonic studies have shown a spectrum of fault slip behavior along different sections of the Philippine Fault. The location of several major modern and historical earthquakes are associated with northern and southern splays of the Philippine Fault (Bautista & Oike, 2000). However, only a handful have been determined to have produced surface ruptures, like the 1990 magnitude M_w 7.7 Luzon (Punongbayan et al., 1992; Silcock & Beavan, 2001), the 1973 M_s 7.3 Ragay Gulf (southern Luzon) (Tsutsumi et al., 2015), and the 1879 M_s 6.9 and 2017 M_w 6.5 Surigao (Mindanao) (Perez & Tsutsumi, 2017; PHIVOLCS, 2018) earthquakes. The central section of the fault (from 10–12.5°N) is known for clusters of moderate to strong earthquakes (~M 5–6), including the surface-rupturing 2003 M_s 6.2 Masbate earthquake (Bacolcol et al., 2005). It has also been suggested that the Masbate earthquake was followed by postseismic afterslip (Besana & Ando, 2005). In addition, directly south of Masbate, aseismic slip on the island of Leyte was first quantified from campaign GPS surveys around the Tongonan geothermal area in northern Leyte. Fault-parallel aseismic slip rates on the surface range from 2.6 cm/yr (Duquesnoy et al., 1994) to 3.5 cm/yr (Duquesnoy, 1997; Prioul et al., 2000). As previously mentioned, the 6 July 2017 M_w 6.5 earthquake ruptured the section of the fault where these surveys were conducted.

2.2. Seismotectonics of Leyte Island

The Philippine Fault goes through the island of Leyte from its northern to its southern shores, with a marked 150-km-long onshore trace. At the latitude of the island, the fault crosses the volcanic arc associated with the Philippine Trench subduction zone (Barrier et al., 1991) (inset of Figure 1). The fault is especially clear on narrow linear valleys and portions that cut through Quaternary volcanoes and the central highlands (Allen, 1962; Aurelio et al., 1993; Lagmay et al., 2003; Tsutsumi & Perez, 2013; Willis, 1944).

Active fault maps, based on topographic data from aerial photos and 90-m resolution global digital elevation models (PHIVOLCS, 2016; Tsutsumi & Perez, 2013), reflect the main fault trace as a linear feature along the length of the island, with a bend near Tongonan village. There, subparallel secondary faults east of the main trace demarcate a 2- to 2.5-km-wide relay zone that, further south (west of Burauen in Figure 2a), becomes a 4-km-wide left-stepping step-over at around 11°N. Structural field observations and tectonic models expound on localized extension and secondary faulting along this releasing bend (Aurelio et al., 1993; Duquesnoy et al., 1994) and the sigmoidal structures that result from long-term volcano-tectonic interactions (Lagmay et al., 2003). The Leyte Geothermal Production Field in Tongonan has been exploiting the abundant geothermal resources related to the Quaternary volcanoes for commercial energy production since the 1980s. Geothermal exploitation within the fault bend leads to subsidence of up to 3 cm/yr (Apuada et al., 2005).

South of Tongonan, a rift-like morphology can be observed on the wide valleys west of Burauen, which Willis (1944) attributes to be a part of a “Visayan Rift.” Subsequent mapping by Allen (1962) describes the active left-lateral strike-slip kinematics. The most recent work by Tsutsumi and Perez (2013) does not map out structures west of the main trace as active.

Several studies focusing on geothermal energy exploration suggest that the faulting (e.g., Aurelio et al., 1993; Lagmay et al., 2003) and continuous aseismic slip (Caranto & Jara, 2015) on the Philippine Fault in the volcanic area enhances the permeability in the shallow crust, allowing for the outflow of geothermal fluids. Duquesnoy et al. (1994) propose that the high heat flow and the clay alteration of volcanic rocks, due to the hydrothermal activity, might affect the rheology of the fault zone. They postulate that this causes the weakening of the fault zone, which, in turn, promotes aseismic slip.

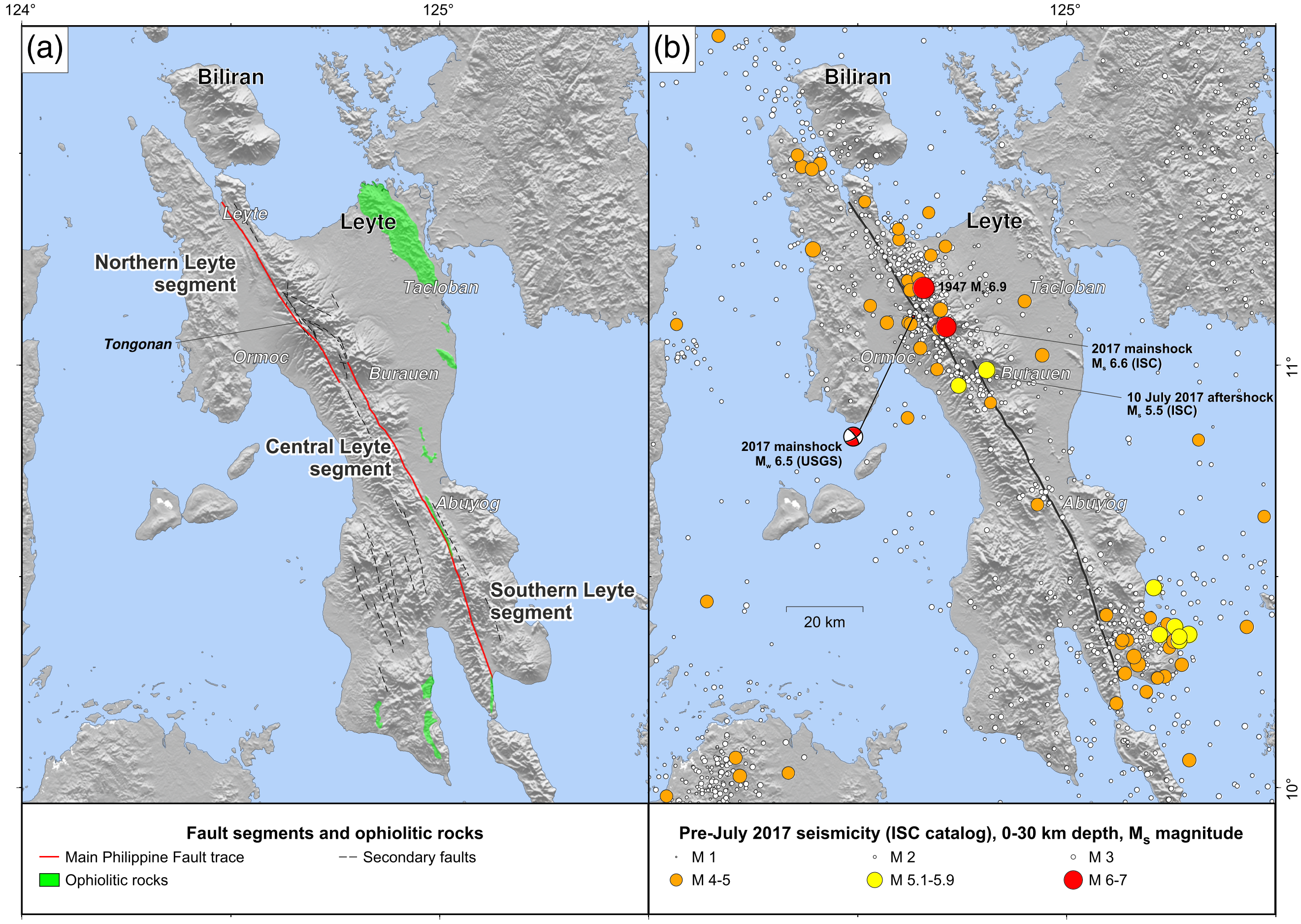

Figure 2. Seismotectonics of Leyte island. (a) Main Philippine Fault segments referred to in the text (red line), along with secondary structures (dashed black lines) and surface exposures of ophiolitic rocks (Aurelio et al., 1993; Guotana et al., 2018; Suerte et al., 2005). (b) Instrumental seismicity (1984 to July 2017) in Leyte based on the rebuilt International Seismological Centre (ISC) catalog (Storchak et al., 2017). Symbol sizes are scaled according to surface wave magnitude (M_s). The mechanism and location of the July 2017 mainshock reported by the USGS is shown for reference (red beach ball).

The ophiolitic basement is also exposed on the surface in Leyte (Aurelio et al., 1993; Cole et al., 1989; Dimalanta et al., 2006; Guotana et al., 2018; Suerte et al., 2005), as shown in Figure 2. While the mineralogy of serpentinites from ophiolites along the San Andreas Fault has been considered to explain aseismic slip (e.g., Moore & Rymer, 2007), this has yet to be suggested for the Philippine Fault, so we expound on this in detail in the discussion (section 5).

Fukushima et al. (2019) show the along-strike variability of surface aseismic slip rates based on the step change of InSAR-derived surface velocity. However, due to the large magnitude of subsidence in the geothermal area, they are unable to estimate the rate of interseismic aseismic slip where the 2017 earthquake happened.

We focus this paper on two main segments of the Philippine Fault in Leyte, which are primarily based on distinct continuous surface traces: the Northern Leyte Segment (the section of the fault from Leyte town to Ormoc) and the Central Leyte Segment (from Burauen to Abuyog) (Figure 2a). Plotting the reviewed catalog of the International Seismological Centre (ISC; Storchak et al., 2017) of seismic events from 1964 to just before the July 2017 earthquake shows a clustering of seismicity in northern Leyte, which contrasts with what can be seen in central Leyte (Figure 2b). Besana and Ando (2005) have implied that a "large" earthquake in 1608 ruptured the Central Leyte Segment and may suggest that a "seismic gap" exists between Burauen and Abuyog. Bautista and Oike's (2000) review of the preinstrumental historical record of

Table 1
Summary of ALOS SAR Data per Track Used for Interseismic Time Series Analysis and Stacking

Date range	Track	# of acquisitions	# of interferograms	*N* valid[a]
2006/12 to 2011/01	443, Ascending	25	86	50
2006/10 to 2011/01	76, Descending	5	10	6
2008/09 to 2010/12	77, Descending	3	3	2

Note. Dates are formatted as yyyy/mm.
[a] Number of required coherent measurements from interferogram network on a pixel to make a velocity estimate.

earthquakes in the Philippines, however, suggests that the 1608 earthquake had a M_s of 5.0 and a poorly constrained location (i.e., this event only has two reports that could be used as basis for the equivalent Modified Mercalli intensity). In southern Leyte, seismicity broadly clusters to the east of the fault trace.

3. Interseismic (2007–2011) Velocity Field and Aseismic Fault Slip

In this section, we explore the aseismic slip throughout the fault in Leyte including where the anthropogenic subsidence occurs. By deriving high-resolution velocity maps from InSAR data and including a subsidence source in the kinematic inversions, we are able to isolate the strike-slip fault deformation. We generated line-of-sight velocity maps with a spatial resolution of around 100 m in radar range (nominally of higher resolution compared to the 1,500-m resolution velocity maps in Fukushima et al., 2019). This allows us not only to to revisit the surface manifestation of shallow aseismic slip on the fault but also to capture the anthropogenic subsidence in enough detail that corresponds to data from local leveling surveys (Apuada et al., 2005).

3.1. InSAR Data Processing

Using available synthetic aperture radar (SAR) data from ascending and descending passes of the ALOS satellite (Table 1), we analyze the surface deformation on Leyte during the 2007 to 2011 interseismic period. Because there has not been any large earthquake in the area in the 70 yr prior to the 2017 earthquake, we do not expect significant postseismic transient motion, and we can be confident that the ALOS measurements capture only interseismic motion. ALOS L-band SAR data (wavelength, $\lambda = 23.6$ cm) has the advantage of being able to produce coherent interferograms in vegetated areas despite long temporal baselines (e.g., Pousse Beltran et al., 2016; Sandwell et al., 2008), unlike SAR data at shorter wavelengths (e.g., C and X bands).

We used the GAMMA Software to produce unwrapped interferograms from single-look complex images (SLC). For each track, we coregistered all SLCs to a corresponding reference SLC. Reference SLCs for Tracks 443, 76, and 77 were chosen as a compromise between the perpendicular baseline of individual interferograms and overall baseline extent of the whole interferogram network. We first generated interferograms and multilooked them to a pixel size of around 100 m × 100 m in azimuth and range. We used an adaptive spectral filter to improve the signal-to-noise ratio while preserving high-phase gradients (Goldstein & Werner, 1998). We unwrapped the interferograms using a minimum cost flow (MCF) algorithm (Werner et al., 2002) and masked decorrelated pixels (i.e., those with coherence less than 0.4). We manually corrected unwrapping errors between adjacent islands with less than 2π phase jumps and no expected relative motion (i.e., islands that are on the same side of the fault). For removal of the topographic phase and generating a lookup table for geocoding the data, we used an airborne SAR-derived “bare-Earth” digital elevation model (DEM) from the National Mapping and Resource Information Authority of the Philippines (NAMRIA) (e.g., Luzon et al., 2016). For computational efficiency, we downsampled the 5-m resolution NAMRIA DEM to 10-m resolution.

3.1.1. Estimating Surface Deformation Rates

As the temporal coverage of the ascending and descending passes are not uniform (see supporting information Figures S1–S3 for temporal and spatial baselines, and interferogram pairs), we employed different strategies to measure the surface deformation rate. The ascending track has 25 acquisitions between December 2006 and February 2011 and covers the whole length of the fault in Leyte. The two descending tracks that cover the fault have fewer acquisitions. Data from Track 76 encompasses most of central and

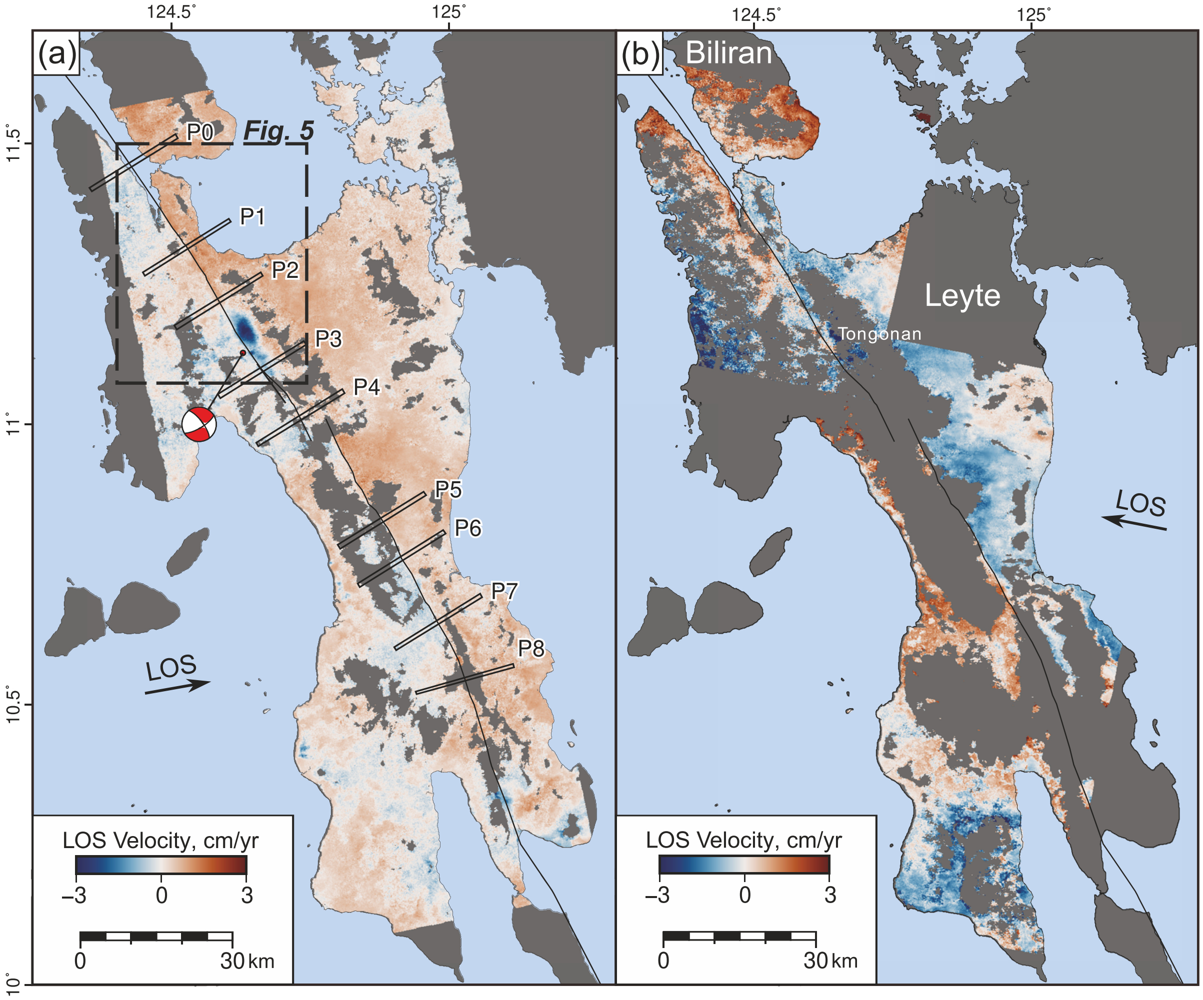

Figure 3. Interseismic surface deformation in Leyte in satellite line-of-sight (LOS) with rates in cm/yr (positive values indicate movement toward the satellite), and the Philippine Fault as the solid black line. Gray areas within the velocity field correspond to pixels masked out due to temporal decorrelation. (a) Surface deformation from time series analysis of ascending ALOS data (Track 443). The 6 July 2017 mainshock (M_w 6.5) location is shown for reference. LOS velocity swath profiles, P0–P8, are in Figure 4. (b) LOS displacement rate derived from stack of ALOS descending interferograms (Tracks 76 and 77).

southern Leyte and has five acquisitions from 2006 to 2011. Track 77, which covers northern Leyte and Biliran, has only three acquisitions between 2008 and 2011.

For the ascending track, we followed an N-SBAS (Small Baseline) time series analysis approach implemented in the Generic InSAR Analysis Toolbox (GIAnT; Agram et al., 2013). This method allows the estimation of velocities in areas that have decorrelated signals in some interferograms but have at least a specific number of coherent measurements (N) in the interferogram network (e.g., Doin et al., 2011; Jolivet et al., 2012). For the time series inversion, we manually selected 86 interferograms with no apparent nonlinear phase ramps, which are usually due to ionospheric perturbations (Gomba et al., 2016). The resulting interferogram network still covers 4 yr of data (from 2007–2011, as shown in supporting information Figure S1). We estimated the LOS velocity for pixels where more than 50 interferograms are unwrapped, assuming a linear rate. We included a step function in time to remove the coseismic signal from a M_w 5.3 earthquake in southern Leyte that has visible surface deformation off the Philippine Fault. Prior to inverting for the LOS velocity, we applied atmospheric corrections based on the European Centre for Medium-Range Weather Forecasting ERA-Interim models (Jolivet et al., 2014). We also removed planar ramps on individual interferograms and corrected for DEM errors. The resulting velocity map has a mean root-mean-square error of 1.3 cm/yr (supporting information Figure S4a).

For the descending tracks, we did not perform a complete time series analysis to derive deformation rates as we do not have enough acquisitions. Instead, we estimated the average LOS displacement rate, $\dot{\phi}_d$, through a simple yet robust *stacking* approach, implemented in GAMMA, from the unwrapped interferograms. For N number of interferograms, the algorithm uses the temporal baseline, Δt_j, of the respective j interferograms as a weight for LOS displacement, ϕ_j, to derive $\dot{\phi}_d$, as

$$\dot{\phi}_d = \frac{\sum_{j=1}^{N} \Delta t_j \phi_j}{\sum_{j=1}^{N} \Delta t_j^2}. \tag{1}$$

Similar to the N-SBAS time series approach, this formulation lets us estimate deformation rate on pixels that have coherent signals in N number of interferograms in the stack. We set N to to be more than half the total number of interferograms of each stack (Table 1). The mean standard deviation for the descending Tracks 76 and 77 stacks are around 1.1 and 0.9 cm/yr, respectively (supporting information Figure S4b).

3.1.2. Deriving Subsidence From InSAR

The LOS velocity maps show a sharp velocity gradient across the Philippine Fault (Figure 3). We measure 0.2 to 0.9 cm/yr difference in the ascending LOS velocity across the fault with a step-like function right on the fault (Figure 4). Motion is compatible with the left-lateral sense of slip on the fault, as shown by the opposite LOS deformation rate observed on ascending versus descending tracks. We also observe an elliptical deformation feature that is most likely related to subsidence adjacent to the fault. Leveling surveys by Apuada et al. (2005) indicate up to 18 cm of subsidence in the Leyte Geothermal Production Field between 1997 and 2003. They associate this phenomena with net mass loss from energy production, as extraction rates exceed fluid reinjection rates. Since the geothermal production is ongoing, it is likely that subsidence still occurs in the area.

With InSAR displacements from multiple LOS directions, we can derive horizontal and vertical velocity components and provide new measurements of subsidence. The off-nadir LOS of the SAR satellites makes InSAR most sensitive to vertical deformation; nonetheless, it is also possible to derive the eastward and northward component of horizontal motion (e.g., Fialko et al., 2001; Wright et al., 2004). As we lack a third velocity vector, however, we are unable to independently constrain the eastward and northward components of horizontal motion. We can instead project the east and north horizontal components of the InSAR LOS to the dominant horizontal direction of movement around the fault (as in Lindsey et al., 2014; Tymofyeyeva & Fialko, 2018).

Given the LOS velocity from ascending ($\dot{\phi}_a$) and descending ($\dot{\phi}_d$) tracks, we inverted for vertical and fault-parallel velocity components, V_v and V_f, respectively, as

$$\begin{bmatrix} \dot{\phi}_a \\ \dot{\phi}_d \end{bmatrix} = \begin{bmatrix} e_a \sin(\alpha) + n_a \cos(\alpha) & u_a \\ e_d \sin(\alpha) + n_d \cos(\alpha) & u_d \end{bmatrix} \begin{bmatrix} V_f \\ V_v \end{bmatrix}, \tag{2}$$

where e, n, and u are the east, north, and up components, respectively, of the unit vector pointing toward the satellite. α is the average strike of the Philippine Fault (328°), which corresponds to its large-scale strike-slip nature, and is, to first order, consistent with the GPS observations (Duquesnoy, 1997) (Figure 1).

To maintain temporal consistency, we derived the ascending LOS displacement rate for this inversion from stacking interferograms (as in section 3.1.1) that cover the same time period as the descending track (2008–2010). The derived fault-parallel and vertical velocities are shown in Figure 5.

3.2. Manifestation of Surface Aseismic Slip

The LOS velocity map from the ALOS ascending track data shows a clear discontinuity across the fault (Figures 3a and 4, Profiles P0, P1, and P4 to P7). This is apparent on a ~100-km-long section of the fault, albeit discontinuously, between 10.5°N and 11.5°N. Comparing the LOS velocity with the elevation on the same profiles suggests that this step change does not correlate to elevation gradients. The contrast in surface velocity, however, coincides with well-preserved fault scarps and most of the mapped surface trace of the Philippine Fault (as in Tsutsumi & Perez, 2013) in the northern and central sections of the island. We therefore attribute the velocity step to aseismic slip on the surface. Surface deformation derived from the

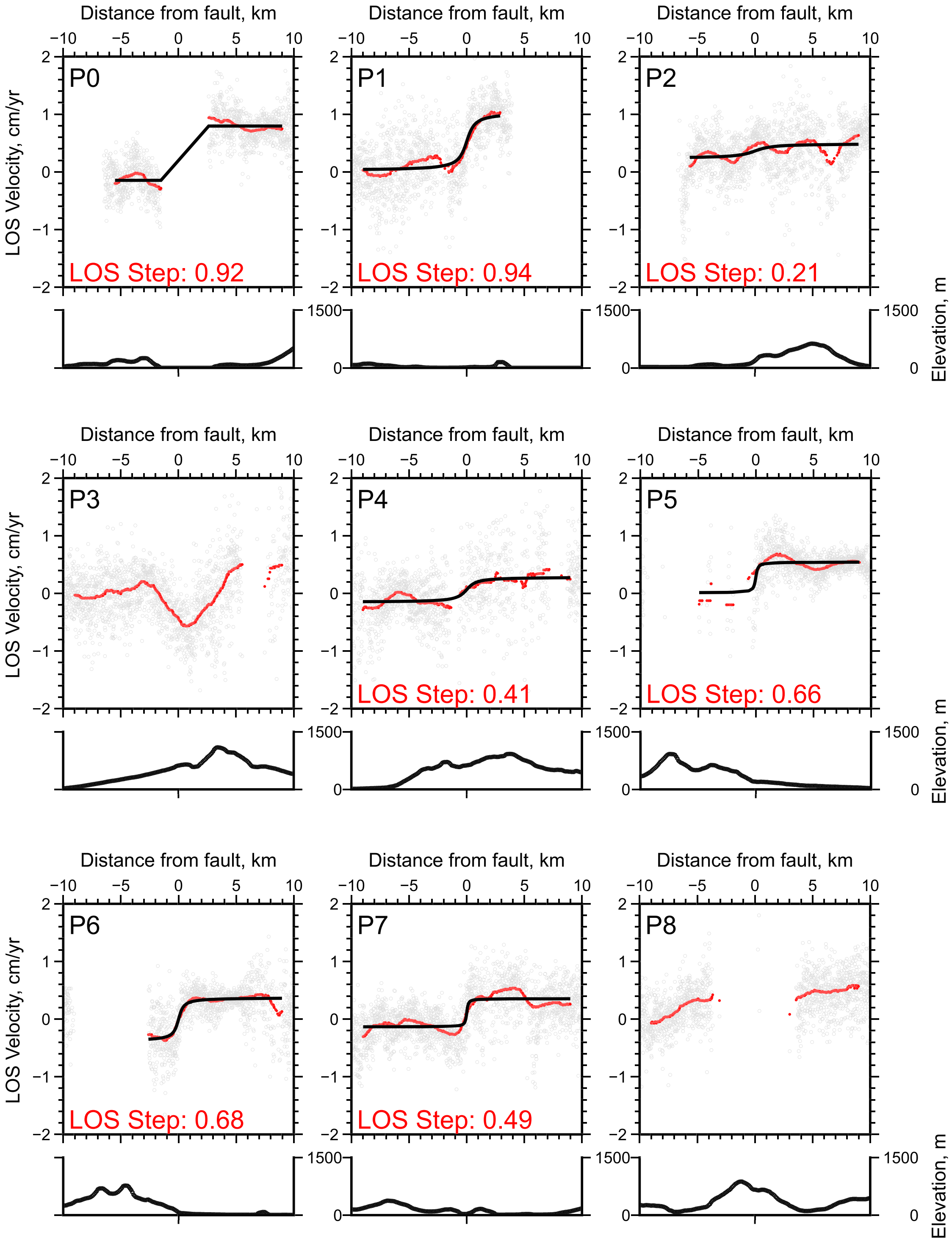

Figure 4. ALOS ascending track (443) LOS velocities and step change (in cm/yr) within 20-km-long, 1-km-wide swath profiles centered on the Philippine Fault in Leyte (see Figure 3 for location). Corresponding elevations are shown below each profile. Gray dots and red line represent the LOS velocity and median value, respectively. Black lines indicate the step function fit to the median LOS velocity (see Appendix A).

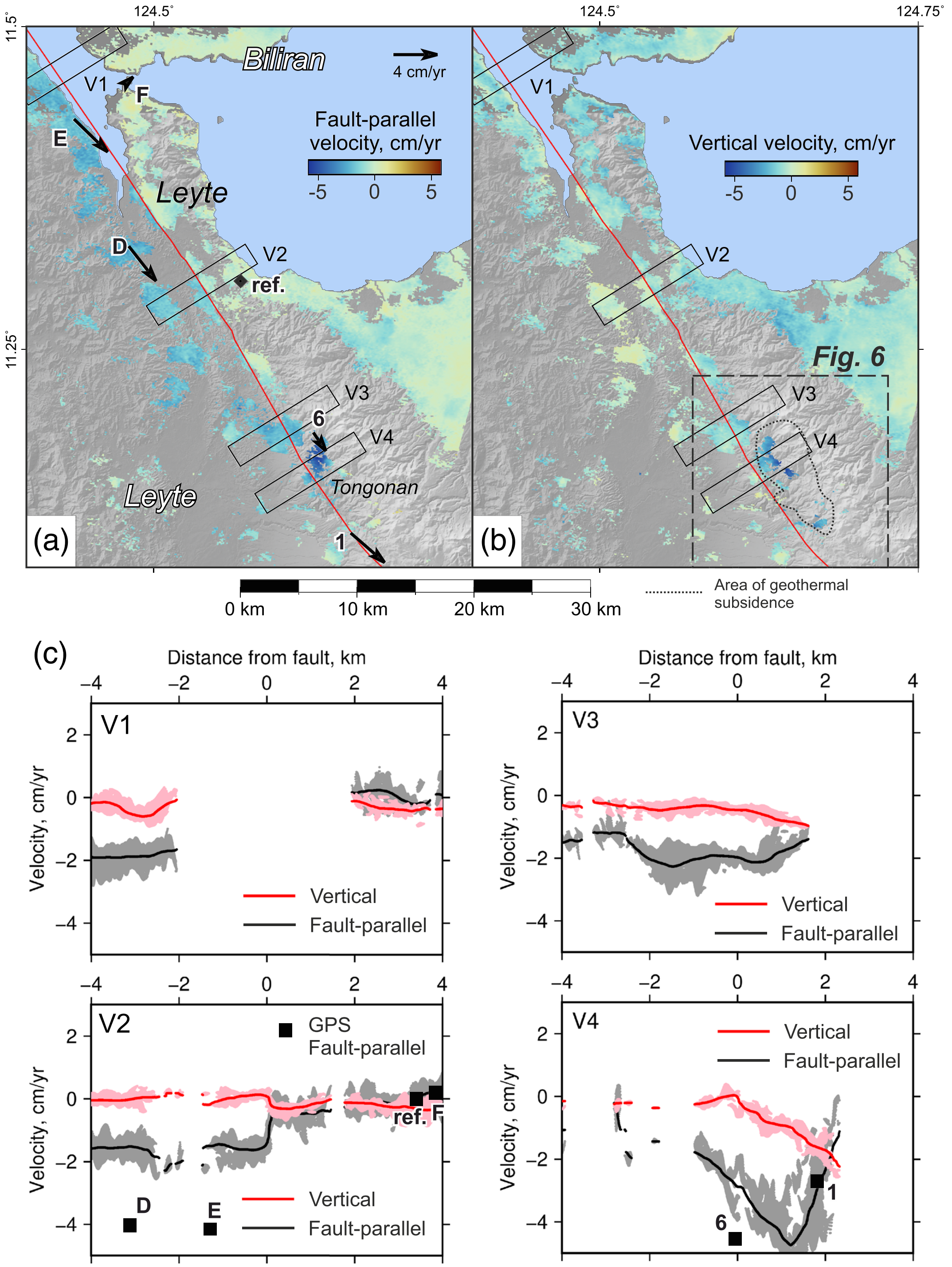

Figure 5. Estimated fault-parallel and vertical velocity in northern Leyte. (a) Fault-parallel velocity from InSAR analysis. Black boxes show the spatial extent of swath Profiles V1 to V4. Black vectors are GPS velocities from Duquesnoy (1997) (same as Figure 1) relative to the reference station (black diamond), with station names outlined in white. (b) Same, but showing the vertical velocity and the geothermal subsidence area (based on Apuada et al., 2005) in Tongonan (dotted outline). (c) Profiles of fault-parallel velocity (gray: data, black: median) and vertical velocity (pink: data, red: median) from Swaths V1–V4. V2 shows a clear step function in fault-parallel velocity right on the fault, which is absent in V3. This suggests that shallow aseismic slip on the fault occurs near the surface at V2, but not on V3. The fault-parallel component of Duquesnoy (1997) GPS data (black squares) are shown in provile V2 for reference.

descending track acquisitions (Figure 3b) has a lot more spatial variability and observation gaps. This is likely due to consistent temporal decorrelation of interferograms, resulting to less than the N number of observations required to estimate the average velocity. We nevertheless still observe a contrast in the descending LOS velocity across the fault, as also noted by Fukushima et al. (2019). We describe below in more detail the deformation field, from north to south.

North of 11.4°N, while the Philippine Fault disappears below water in the strait between Leyte and Biliran, we observe a clear difference in velocity between the two islands, which are on opposite sides of the fault (P0 in Figures 3 and 4). Although unwrapping across water requires the assumption that no significant phase jump exists between landmasses, we are confident that the consistency between surface deformation rates in Leyte and Biliran suggests our velocity field is robust. In the town of Leyte, just north of Profile P1, field observations and anecdotal reports suggest that roads, houses, and other concrete structures show signs of left-lateral displacement even if there are no significant seismic events (supporting information Figures S5b and S5c). Profiles V1 and V2, in Figure 5, highlight the fault-parallel motion across the fault between the islands of Leyte and Biliran and onshore in northern Leyte, respectively. They both correspond to left-lateral motion, which on Profile V2 is a clear step function of 2 cm/yr right on the fault. This signifies that, for this time period at least, the northern section of the fault in Leyte slipped aseismically at around the long-term rate near the surface. The GPS fault-parallel velocities from Duquesnoy (1997) (black squares in Profile V2) appear to suggest faster motion than the InSAR data across the fault. This may reflect temporal variations on the interseismic slip rate in this location, but the sparse GPS data coverage makes it difficult to make robust inferences.

Contrast in surface velocities across the Philippine Fault is less prominent on Profile P2 (Figure 4), north of Tongonan. The derived fault-parallel surface velocity also shows no discontinuity across the fault in this area (Figure 5c, Profile V3), possibily indicating that the fault is locked near the surface. Another possibility is that the aseismic slip signal between Profiles P2 and P3, if any, might be obscured by the subsidence-related deformation in Tongonan (Profile V4 in Figure 5c). Finally, significant surface ruptures related to the 6 July 2017 M_w 6.5 earthquake are found just south of Profile V4 (PHIVOLCS, 2017).

Along the central highlands in Leyte, temporal decorrelation leads to gaps in the LOS velocity maps near the fault. Still, LOS velocity steps are visible across the fault from Burauen down to Abuyog, between 11°N and 10.6°N (Profiles P4 to P7 in Figure 3). In the field, continuous and slow offset of roads in Abuyog have been documented by Tsutsumi et al. (2016). One of these roads has been repaved recently, but it appears the prerepavement displacement has been preserved (supporting information Figure S5d).

South of Abuyog, no clear contrast in the LOS velocity is observable (e.g., P8 in Figure 3). However, it does not necessarily mean that the fault does not slip aseismically near the surface. The ascending track LOS is orthogonal to the fault in this area, which makes fault-parallel deformation, if it exists, unresolvable. Looking at the descending data, which has a LOS oblique to the fault, there does appear to be a difference in the far-field velocities across the fault. However, we lack sufficient coherent data to be able to resolve the deformation rates closer to the fault. The off-main trace faulting in southern Leyte (Figure 2a) might also mean that deformation is more distributed across a wider area.

3.3. Subsidence in Tongonan

Our analysis of LOS surface velocities makes it apparent that to delineate the expression of shallow aseismic slip, we need to understand the contribution of the subsidence source to the deformation field adjacent to the fault. The vertical displacement rate, as seen in Figure 5b, shows subsidence in an area previously monitored by leveling surveys (Apuada et al., 2005). We estimate up to ~2.5 cm/yr of subsidence (Profile V4, Figure 5c), which is slightly less than the reported ~3 cm/yr of maximum subsidence from the geothermal survey by Apuada et al. (2005). This discrepancy may be due to temporal variations in net mass loss, especially as a gradual decrease in extraction rates since the early 2000s has been reported (Hazel et al., 2015). We also note a significant amount of horizontal motion in the subsidence area (Profile V4 in Figure 5c), but in the opposite direction of that corresponding to left-lateral slip on the fault (see Profiles V1 and V2, Figure 5c). Since both ascending and descending tracks are not consistently coherent in this area, we cannot derive meaningful horizontal and vertical deformation rate maps there. However, the apparent horizontal motion in Profile V4 may be related to the subsidence, in which case, it represents the surface moving toward the area of peak subsidence.

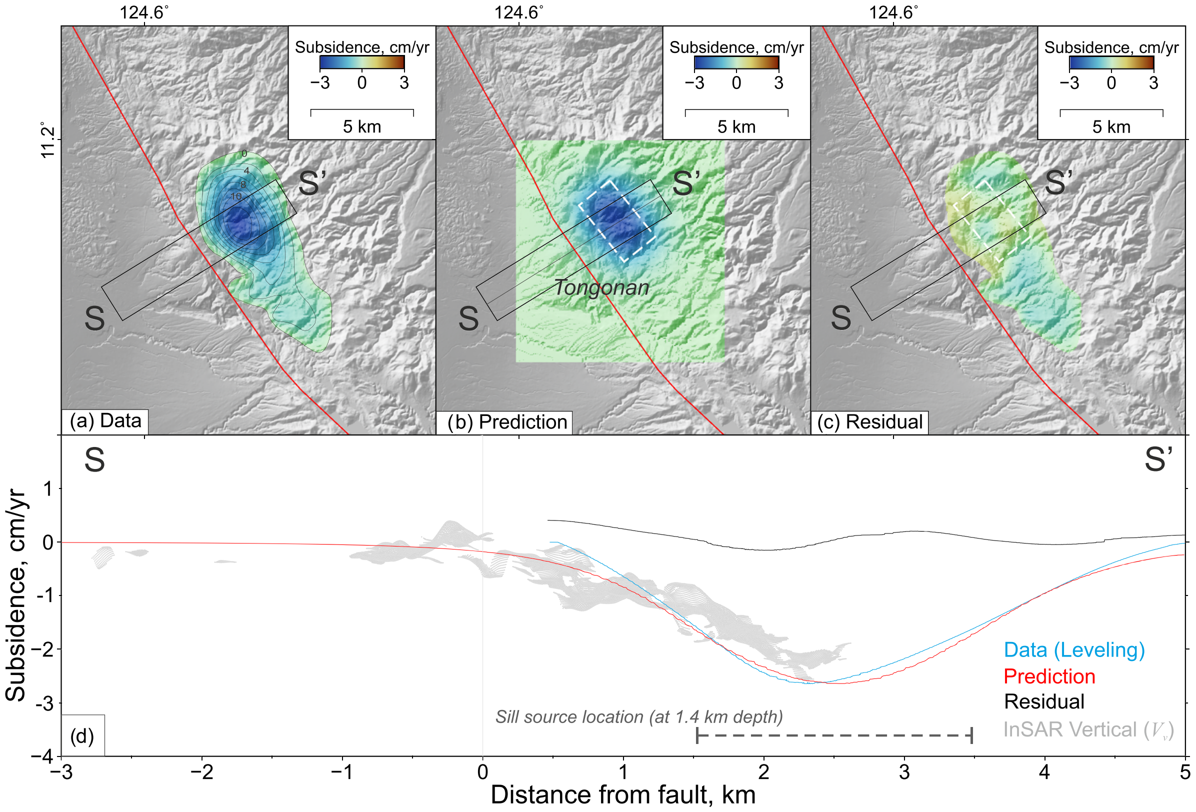

Figure 6. Subsidence data, model prediction, and residuals from modeling using leveling data (Apuada et al., 2005). (a) Interpolated subsidence rates based on leveling contours, with extent of swath profile, S-S′ (black rectangle). The outermost contour represents zero subsidence as published in Apuada et al. (2005), and each contour interval represents 0.2 cm/yr of subsidence. (b) Predicted subsidence from the optimal source model geometry, with the surface projection of the sill source (white dashed polygon). (c) Residual deformation (the difference between data and predictions). (d) Profiles of median subsidence data (blue), prediction (red), and residuals (black) in Swath S-S′. Vertical surface velocity (V_v) in the swath from InSAR decomposition (gray points) and the location of the sill (dashed line) at the swath midsection also shown for reference.

3.4. Modeling Deformation Sources

Surface observations indicate that the Philippine Fault slips aseismically up to the surface for a significant fraction of its Leyte section. The geothermal production field also leads to surface deformation in Tongonan. Hence, in our attempt to model the distribution of aseismic slip on the fault, we need to account for the contribution of a subsidence source to the interseismic deformation field. We describe in this section the details of our modeling approach, where we first determined a simple horizontal rectangular source for the subsidence from leveling surveys conducted in 1997 and 2003 (section 3.4.1). While we do not aim to explain the subsidence mechanism, deflationary elastic source models can be used to explain compacting or deflating geothermal sources (e.g., Receveur et al., 2019). Then, using this subsidence source and a fault geometry based on the known trace of the Philippine Fault, we jointly solved for the rates of subsidence source deflation and aseismic slip on the fault using the LOS velocity maps derived over the 2007–2011 period (section 3.4.3). Our main assumption is that the geometry of the source of subsidence did not change from the time of early leveling surveys (i.e., the data we use to infer the geometry of the source) to the time of SAR observations.

We followed a probabilistic (Bayesian) approach to invert for the various parameters of our model. The linear problem, $\mathbf{d} = \mathbf{Gm}$, allows us to invert for a vector of unknown model parameters, $\mathbf{m}$, from a vector of surface observations, $\mathbf{d}$ (e.g., InSAR and leveling data), and a Green's function matrix, $\mathbf{G}$, assuming a homogeneous elastic half-space (Okada, 1985). With Bayes theorem, we are able to derive the a posteriori probability distribution (also called posterior probability density function, PDF), of the model parameters given the data, $p(\mathbf{m}|\mathbf{d})$, as

$$p(\mathbf{m}|\mathbf{d}) \; \alpha \; p(\mathbf{m}) \, \exp\left[\frac{1}{2}(\mathbf{d}-\mathbf{Gm})^T \mathbf{C}_d^{-1}(\mathbf{d}-\mathbf{Gm})\right], \tag{3}$$

Table 2
A Priori Bounds and Inversion Results for a Horizontal Rectangular Source for the Observed Subsidence (From Leveling Surveys)

	Length (m)	Width (m)	Depth (m)	Strike (°)	Opening (cm/yr)	X (m)	Y (m)[b]
Lower bound	500	300	100	300	−10.0	−500	4,000
Upper bound	10,000	5,000	5,000	359	10.0	4,000	2,500
Optimal[a]	3,516	1,939	1,377	321.2	−4.2	1,022	577.1
2.5%	1,338	1,838	958.7	302.1	−9.8	151.2	−1,302
97.5%	8,536	1,737	3,588	356.9	−1.5	2,436	1,610

Note. We give the optimal values[a], and 2.5% and 97.5% percentile bounds of the posterior distributions (shown in Figure 7).
[a] Maximum a posteriori probability [b] X and Y refer to the position in eastings and northings of the center of the northeastern edge of the sill relative to the reference point (124.641208°E, 11.164502°N). Opening is negative for a deflating source.

where $p(\mathbf{m})$ is the prior PDF of the model parameters, which can be defined from a priori understanding of the physics of the problem (e.g., Bagnardi & Hooper, 2018; Jolivet, Simons, et al., 2015; Minson et al., 2013). For example, to model slip on the Philippine Fault, we can define prior PDFs that correspond to the known kinematics of the fault, that is, left-lateral strike slip. C_d is a variance-covariance matrix that describes the noise in the data (as in Jolivet et al., 2012; Lohman & Simons, 2005; Sudhaus & Jónsson, 2009, among others). We then can sample models ($\mathbf{m}$) to describe the posterior PDF and evaluate the model statistics (e.g., in terms of the mean and uncertainties of the PDF). We apply two different approaches to sample two different PDFs in the following sections, first to recover the geometry of the source of subsidence and then to derive the distribution of aseismic slip along the fault.

3.4.1. Inversion for the Subsidence Source Geometry

We used the subsidence measured from leveling surveys, done by Apuada et al. (2005) between 1997 and 2003, to infer the geometry of the underground source of subsidence. This allowed us to constrain the source geometry independently from the InSAR data and use the vertical velocity derived from InSAR as verification instead. We avoided inverting for the subsidence source geometry from the derived InSAR velocity maps as this might lead to parameter overfitting to the complex deformation field in the InSAR line-of-sight. We excluded the leveling data in the joint inversion of fault and subsidence deformation rates. As the raw leveling data no longer exists, we digitized the subsidence contours from Apuada et al. (2005) and interpolated a raster of the subsidence rate using GRASS GIS (GRASS Development Team, 2017) (Figure 6a). Further, the elongated elliptical shape of the subsidence suggests a northwest trending source. We therefore inverted for a horizontal rectangular source (sill) in an elastic half-space (Okada, 1985) (Figure 6b and Table 2).

We constrained the source parameters using the Geodetic Bayesian Inversion Software (GBIS; Bagnardi & Hooper, 2018). We determined the optimal source parameters, including length, width, depth, strike, position, and rate of opening. GBIS uses a Markov chain Monte Carlo (MCMC) sampling, controlled by a Metropolis-Hastings algorithm, to approximate the posterior PDF from the parameter space based on a priori assumptions of the source (Bagnardi & Hooper, 2018, and references therein). The prior PDFs are expressed as uniform probability density functions. As the subsidence source in Tongonan is unknown, we set broad bounds for the prior PDFs to allow exploration of different sill geometries between 0 and 5 km depth (a priori bounds are summarized in Table 2).

We generated 10^6 samples of the posterior PDFs of the source parameters. The first 20,000 iterations of sampling, wherein the GBIS fine-tunes the ideal step size for the random walk in the parameter space for the succeeding samples (Bagnardi & Hooper, 2018), are excluded from the posterior PDFs. The maximum a posteriori probability is taken as the optimal solution from the whole distribution. For spatially continuous data (e.g., InSAR), GBIS also considers the uncertainties of the data in evaluating the posterior probability based on empirical estimation of variance and range (correlation distance) from semivariograms of the noise outside of deforming areas (e.g., Lohman & Simons, 2005; Sudhaus & Jónsson, 2009). As our subsidence data are spatially continuous but do not have far-field information, we arbitrarily assumed a variance (σ^2) of 5 cm^2/y^2 and a range (λ) of 1 km. The former is larger than the observed subsidence gradient (~3 cm/yr), while the latter is smaller than the spatial extent of the data.

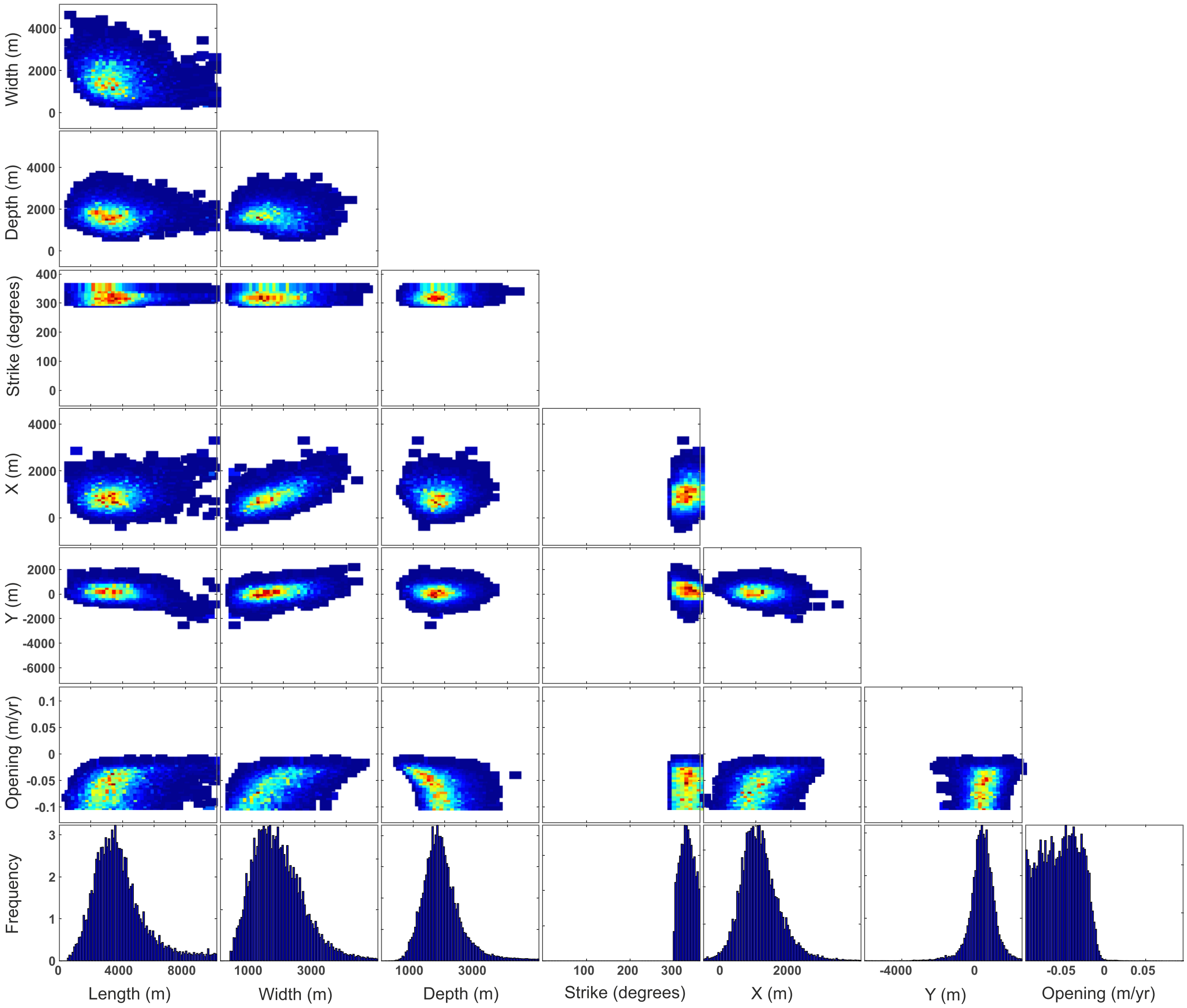

Figure 7. Posterior distribution and joint probabilities of subsidence source parameters from inversion with leveling data. Parameters include length, width, depth, strike, position (*X* and *Y*) relative to reference point, and rate of opening. Cooler colors correspond to lower frequency, and warmer colors indicate higher frequency. See Table 2 for the summary of the statistics of the inversion.

The results show an optimal sill geometry and negative opening (deflation) that largely captures the magnitude and pattern of subsidence (Figures 6). The observed subsidence can be explained by a northwest striking sill source at around 1.4 km depth from the surface, with deflation reaching 4.2 cm/yr (Table 2). The source depth coincides with the depth of the bottom of most wells in the Leyte geothermal production field (i.e., approximately between 1 and 2 km Apuada et al., 2005; Prioul et al., 2000, as displayed in supporting information Figure S6); hence, the probable depth of compaction that can result from geothermal fluid extraction (for a similar geothermal case in Iceland, see Receveur et al., 2019). Based on the joint marginals (Figure 7), we observe that the source geometry parameters are well constrained, with only a slight bias (or correlation) between the sill width and its location. The opening parameter negatively correlates with the width, length, and depth (between 1.2 and 2 km) of the source. The negative correlation between depth and opening means that a deeper source with a larger deflation could predict the observations on the surface as well as a shallower source with smaller deflation. Such bias is expected from the formulation of elastic dislocations and cannot be resolved with surface deformation data only. The fault-perpendicular profiles in Figure 6d show that the extent of the predicted subsidence is slightly wider than the observations, so the source might be slightly shallower. Nevertheless, we find that the extent of deformation and the location

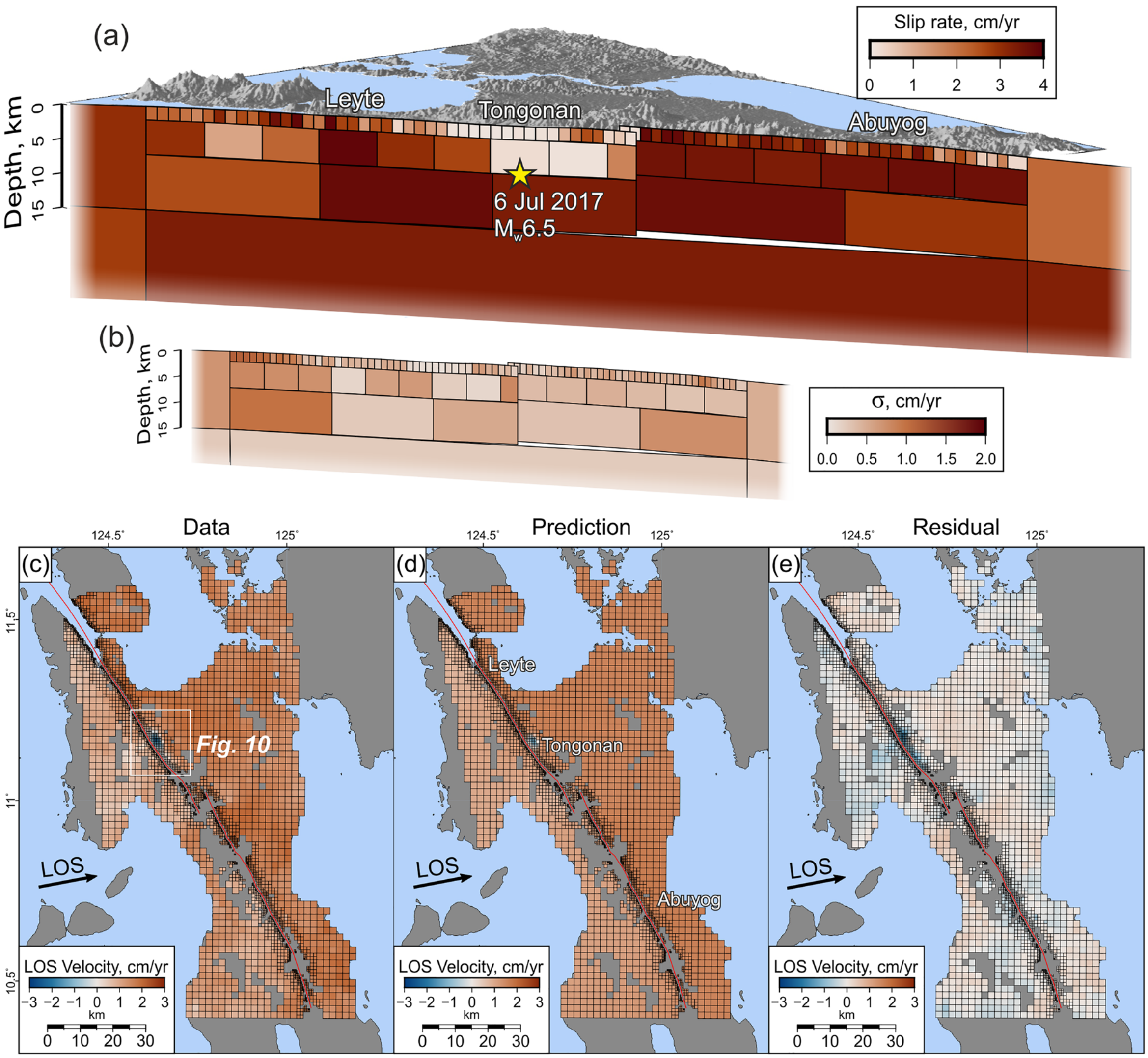

Figure 8. Rate and extent of aseismic slip on the Philippine Fault in Leyte and model fit. (a) Mean of posterior PDF of aseismic slip, in cm/yr, with darker colors indicating faster slip. Star: hypocenter of the July 2017 M_w 6.5 earthquake. (b) Standard deviation of posterior PDF. (c–e) Downsampled ALOS ascending Track 443 InSAR line-of-sight (LOS) velocity data, mean model prediction, and residuals. White square: extent of Figure 8, which shows fit of model to the data in Tongonan. Red line: faults included in model inversion. For the fit of model predictions to descending data, see supporting information Figure S8.

of the optimal model's predicted peak subsidence rate is similar to the vertical velocity component derived from the InSAR data (as shown by the red line and gray dots, respectively, in Profile S-S′, Figure 6d). The root-mean-square of the residuals (Figure 6c) is 0.2 cm/yr. These give us some confidence that the sill-like elastic subsidence source is a useful model to adopt for joint inversion with fault slip.

3.4.2. Fault Parametrization

We then defined the geometry of the fault in the joint inversion for aseismic slip and subsidence deformation rate. Given the regional-scale strike-slip nature of the Philippine Fault, we assumed a vertical fault with the along-strike geometry based on existing active fault maps (Tsutsumi & Perez, 2013), modified to match the fault scarps and linear valleys observable from the 5-m resolution NAMRIA DEM. We reflected the left-stepping nature of the fault as two separate segments—the Northern Leyte and the Central Leyte Segments.

From 0 to 15 km depth, we divided the fault into rectangular patches with increasing patch sizes in three rows (see Figure 8 for the shallow fault geometry).

We explored different discretizations through qualitative trial-and-error tests (e.g., Sagiya & Thatcher, 1999), increasing the size variability from uniform 2 × 2 km square patches. We adopted the variable patch size distribution that balances the ability to capture the heterogeneity at the shallowest sections of the fault (represented by smaller patches at the surface), the decreasing resolution with depth of inversion from surface data, and the convergence of the Bayesian sampling algorithm (Gombert et al., 2018; Jolivet, Simons, et al., 2015).

The downdip widths are 2 km on the top row, 5 km on the middle row, and 8 km on the bottom row. For the Northern Leyte Segment, the along-strike length from the top, middle, and bottom rows are 2, 10, and 30 km, respectively. We set slightly longer patches on the deeper rows of the Central Leyte Segment to account for the gaps in the surface data along the central highlands. The middle and bottom rows of the Central Leyte Segment have 12- and 40-km-long patches, respectively. At depths greater than 15 km, we introduced a single vertical fault with fewer but much larger patches to effectively mimic surface displacements related to an infinitely deep dislocation source, to capture deep slip below the seismogenic zone (Savage & Burford, 1973). Slip on the "deep" patch reflects the secular rate and predicts far-field displacements due to plate motion across a strike-slip boundary.

3.4.3. Joint Modeling of Aseismic Slip and Deflation From InSAR Data

We used AlTar (e.g., Gombert et al., 2018; Jolivet et al., 2014) to jointly solve for the PDF of slip on the fixed fault geometry and deflation rate on the subsidence source. AlTar is a parallel MCMC solver based on the early CATMIP algorithm (Minson et al., 2013) that benefits from GPU acceleration. This algorithm samples the parameter space, imposed by the prior PDF, using a Bayesian formalism. The sampling provides an ensemble of probable models that fit the data within its uncertainties. Furthermore, it does not involve any form of arbitrary smoothing of the solution, often used to regularize the inverse problem. Smoothing of slip between adjacent fault patches is usually a source of discrepancies between deterministic slip models (Duputel et al., 2015; Gombert et al., 2018; Minson et al., 2013, 2014).

We first downsampled the InSAR-derived surface deformation rates with a resolution-based algorithm (Lohman & Simons, 2005). We masked out points within 500 m from the fault to account for uncertainty in the geometry of the fault near the surface. Finally, we excluded data south of 10.6°N where left-lateral slip is likely poorly resolved because the ascending track line-of-sight is orthogonal to the fault fault strike (as discussed in section 3.2). We used empirical exponential function fits to the noise covariograms of each InSAR data set to build the variance-covariance matrix (C_d in Equation 3), as in Jolivet et al. (2012). The empirical standard deviations and correlation lengths, respectively, were 0.1 cm/yr and 6 km for ascending Track 443, 0.2 cm/yr and 4 km for descending Track 76, and 0.3 cm/yr and 3 km for Descending Track 77. The covariograms are shown in supporting information Figure S7.

We assumed a uniform prior PDF for the deflation rate and slip parameters, reflecting our a priori understanding of the left-lateral nature of the Philippine Fault. The fault patches at depths shallower than 15 km had a uniform prior PDF between −0.01 and 4 cm/yr, with positive values denoting left-lateral slip. The negative lower bound was set to allow efficient sampling of zero values. We assigned a normal (Gaussian) prior PDF to the deeper patches, with a mean of 3.0 cm/yr and a standard deviation of 0.25 cm/yr, to reflect the range of published farther-field and long-term slip rates (Barrier et al., 1991; Duquesnoy, 1997; Duquesnoy et al., 1994). As far-field displacement data (i.e., further than ~20 km) is sparse, slip rate on the deeper patches may be less well constrained. Therefore, in order to speed up the sampling and to study only the distribution of aseismic slip consistent with current plate models, we used the Gaussian distribution with rather small standard deviation as the prior PDF.

We obtained more than 100,000 probable models that approximate the posterior PDF. For simplicity, in the following section, we primarily cite the mean and 1σ of the posterior distribution of the parameters (the "mean model," as shown in Figure 8), unless otherwise specified. The mode, skewness, and kurtosis of the posterior marginals (Figure 9) give us further indication of the robustness of inversion results as qualitative indicators of the "shape" of the posterior distribution.

3.5. Results: Variable Aseismic Slip Rate and Apparent Locked Section

The results of the modeling show varying rates of aseismic slip along-strike, with the mean model showing more than 3 cm/yr of slip on several section of the fault (Figure 8). The highest slip rates are present on the onshore Northern Leyte Segment and also along the shallowest patches of the Central Leyte Segment. Along most of the fault, between 2 and 15 km depth, most patches slip rapidly at around 2–3 cm/yr. The model also shows that, below 15 km depth, the fault slips at a rate of 3.3 ± 0.2 cm/yr. This rate is higher than the rates

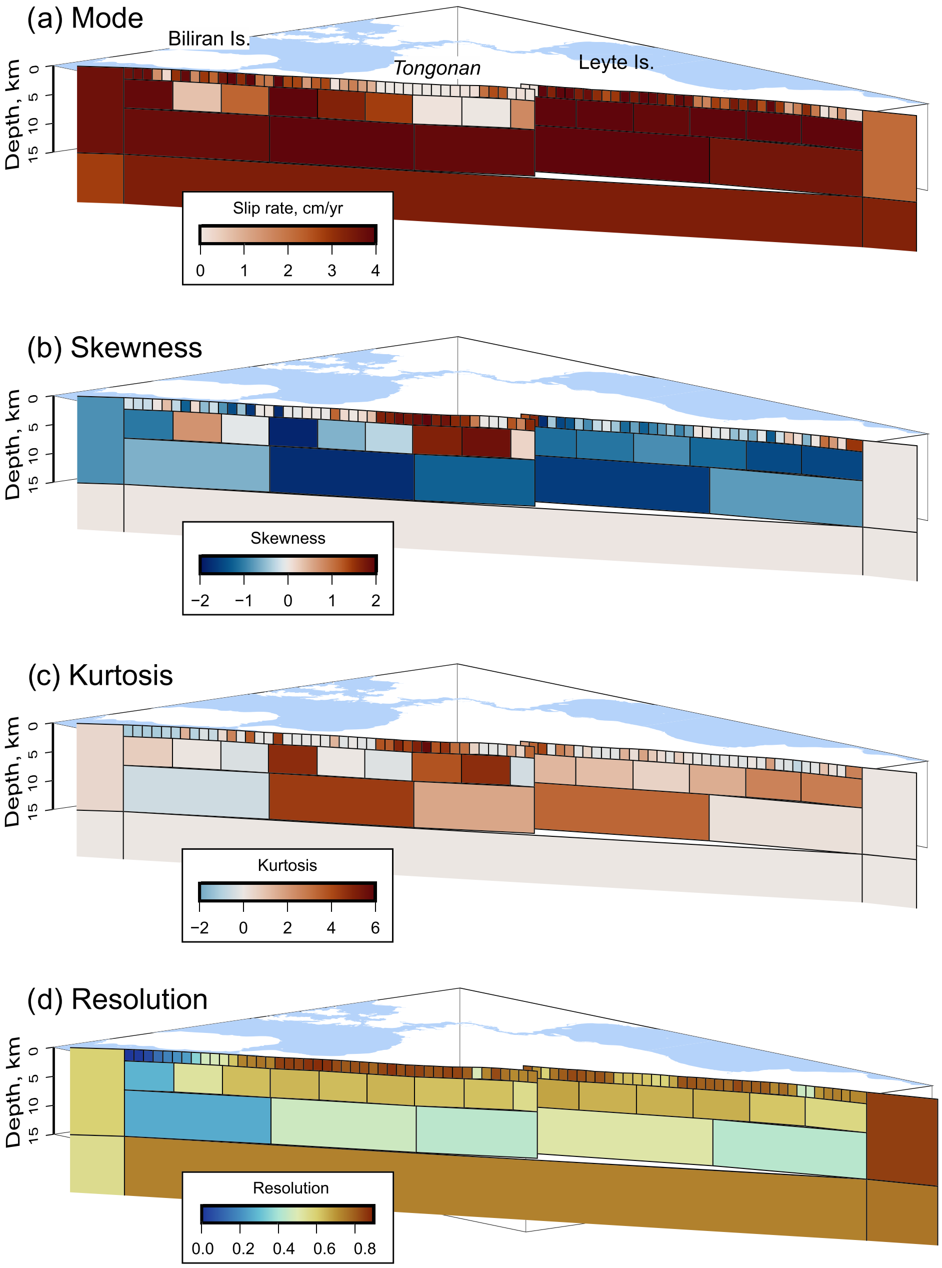

Figure 9. (a) Mode, (b) skewness, and (c) kurtosis of the posterior distribution. (d) Resolution of the inversion on the fault patches, with higher values indicating better resolution (see Appendix B for the resolution analysis).

from plate-scale kinematic analysis (2–2.5 cm/yr Barrier et al., 1991) but is similar to the rates derived from campaign GPS studies in Leyte (2.5–3.5 cm/yr; Duquesnoy et al., 1994; Duquesnoy, 1997).

In contrast, the southern end of the Northern Leyte Segment, hereafter referred to as the Tongonan Segment, appears to slip at a slower rate compared to the rest of the fault. Figure 8a shows that the aseismic slip rate on several contiguous patches from 0 to 7 km depth is close to 0. The small standard deviation (Figure 8b), as well as the mode, skewness, and kurtosis of the posterior PDF (Figure 9a to 9c) provide further indications of very low slip rate in Tongonan across the ensemble of probable models.

This reveals a previously unrecognized section of the fault that has a significant interseismic slip deficit, that is, a locked asperity, which can be a source of earthquakes. The depth of the hypocenter reported by

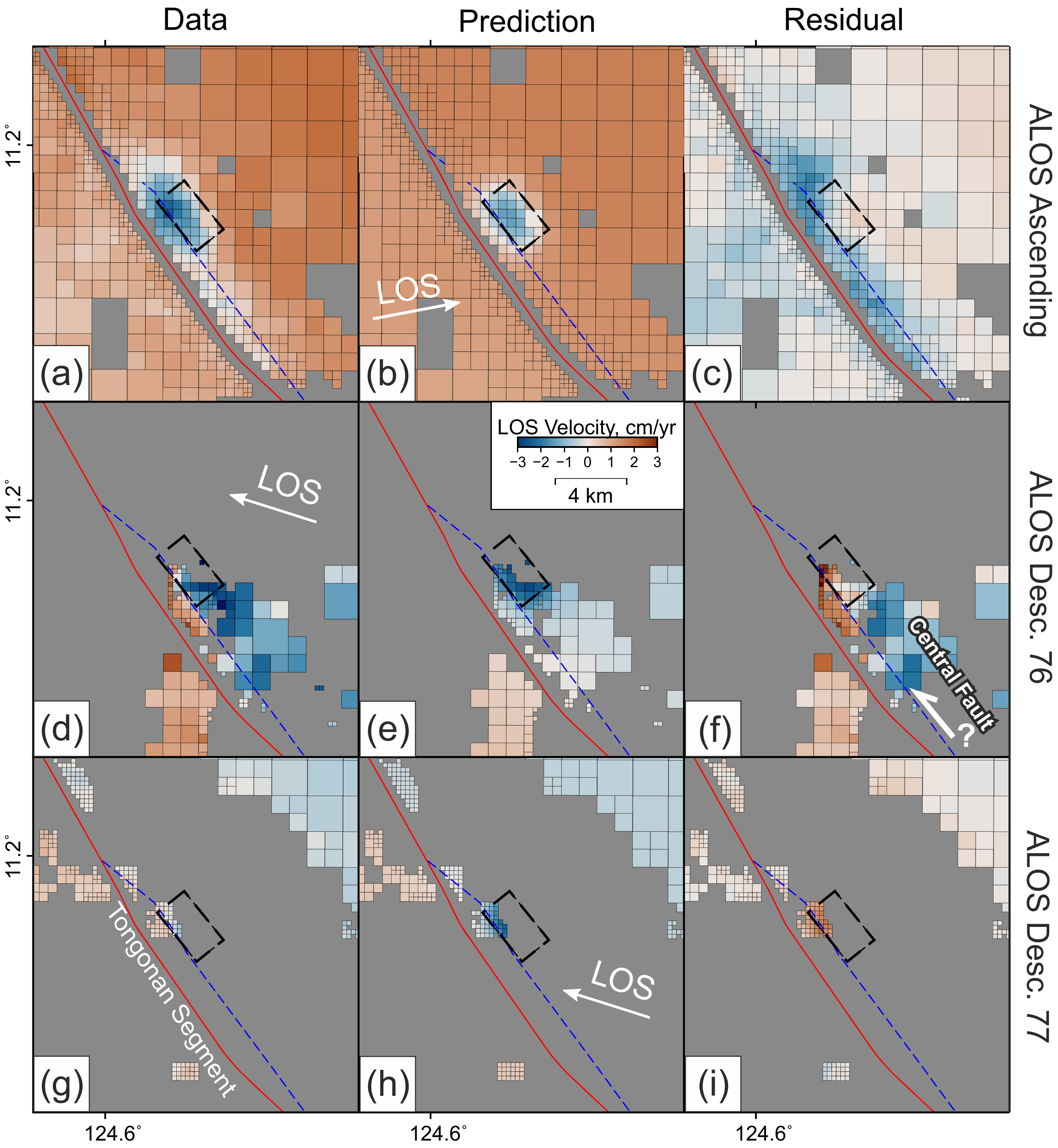

Figure 10. Downsampled InSAR LOS velocity data (left column), model prediction (middle column), and residuals (right column) in the Tongonan area, for ALOS ascending Track 443 (top row, a–c), descending Track 76 (middle row, d–f), and descending Track 77 (bottom row, g–i). Red line: trace of the fault model. Dashed blue line: trace of the Tongonan Central Fault (Aurelio et al., 1993; Prioul et al., 2000). Dashed black rectangle: surface projection of the sill source. The residual velocity across the Tongonan Central Fault branch suggests that this fault is active. The opposite signs of LOS velocity between the ascending and descending tracks suggest that this is likely left-lateral deformation. See text for discussion (section 3.5).

the USGS for the July 2017 M_w 6.5 earthquake is 9 ± 1.8 km, just at the bottom of the locked section (yellow star in Figure 8a). PHIVOLCS, on the other hand, reports a depth of 2 km and a 6.5 surface magnitude (M_s) (PHIVOLCS, 2017). We make further comparisons betweenthe interseismic and coseismic slip models for the July 2017 earthquakes (section 4) in the discussion (section 5).

The resolution matrix indicates that the inversion has resolving power on majority of the patches (Figure 9d, with details on the resolution analysis in Appendix B). The absence of any data points promixal to the shallowest sections of the fault where it goes underwater, in between Leyte and Biliran islands, have much poorer resolution than the patches that correspond to the onshore trace of the Philippine Fault.

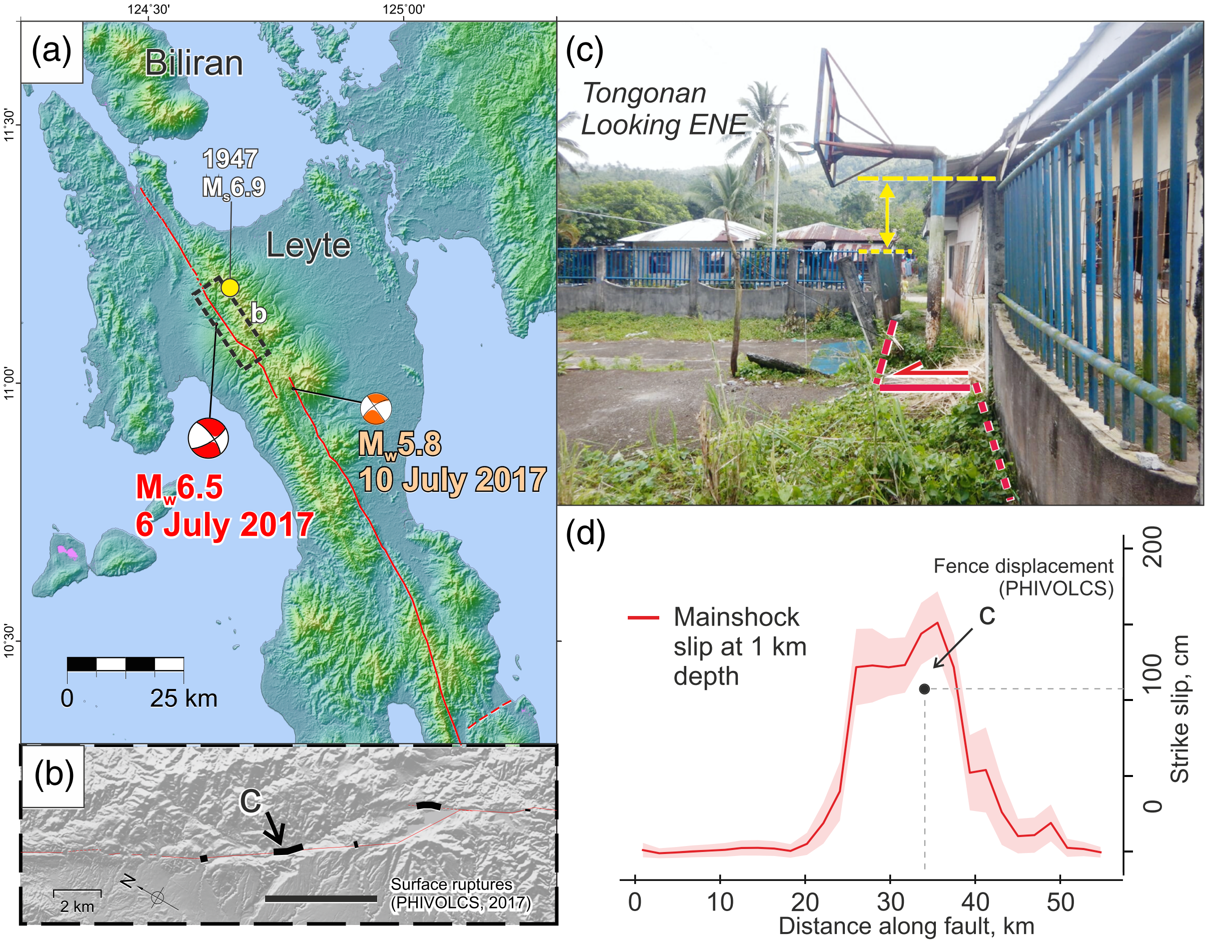

Figure 11. July 2017 earthquakes in Leyte. (a) Map showing the 6 July 2017 M_w 6.5 mainshock (red) and 10 July 2017 M_w 5.8 aftershock focal mechanisms, obtained from the USGS website. Also shown for reference is the location of the 1947 M_s 6.9 earthquake (yellow) from the ISC-GEM catalog (USGS, https://earthquake.usgs.gov/earthquakes/eventpage/iscgem897883/executive). Dashed boxed indicates location of map in (b). (b) Surface ruptures mapped by PHIVOLCS (2017) quick-response team. (c) Displaced concrete fence near the village center of Tongonan, showing left-lateral displacement (red) with a vertical component (yellow) associated with the July 2017 earthquakes, as reported by PHIVOLCS. (d) Along-strike variation of mean (red) and 1σ range (pink area) of posterior strike-slip PDF at 1-km depth from the mainshock model (Figure 14). Distance, in km, is relative to the northern end of the fault in onshore Leyte. Reported displacement by PHIVOLCS (2017) of the fence shown for reference.

The far-field model predictions and residuals of LOS velocity show that our model largely captures the gradient of fault deformation across Leyte (Figure 8d and 8e, respectively). The remaining residuals likely reflect uncorrected atmospheric noise or deformation that is not captured by a simple straight fault model in an elastic half-space.

Closer to the Philippine Fault in Tongonan, however, a linear pattern in residuals is visible, around 2 km east of the main fault trace (Figure 10). This probably is a manifestation of complexity in the deformation field in Tongonan that is not captured by the model. Our sill source model is in this area (dashed black rectangle in Figure 10) and has a deflation rate of 5.4 ± 0.4 cm/yr. This estimate appears to be well constrained as we do not observe obvious trade-offs between the joint marginal PDF of sill deflation and fault slip on adjacent patches (supporting information Figure S9). We, however, cannot exclude the possibilty of a more complex nature of vertical deformation, like subsidence controlled by minor faults. The residuals also might reflect aseismic slip on a secondary, parallel branch of the Philippine Fault—the Central Fault branch (Aurelio et al., 1993; Prioul et al., 2000) (Figure 10f). This seems to be a likely explanation as, when comparing Figure 10c and Figure 10f, the residual velocities between opposing line-of-sights are of different signs across the Central Fault, denoting horizontal motion. We explore this possibility and its implications in the discussion (section 5).

Table 3
Summary of Coseismic Interferograms Used in This Study

Event covered	Date pair	Satellite	Track
M	2017/07/01-2017/07/07	Sentinel-1	61, Descending
A	2017/07/07-2017/07/13	Sentinel-1	61, Descending
M and A	2017/07/01-2017/07/13	Sentinel-1	61, Descending
M and A	2017/06/04-2017/07/15	ALOS-2	136, Descending
M and A	2016/02/13-2017/07/15	ALOS-2	24, Ascending

Note. M: Mainshock, A: Aftershock. Dates are formatted as yyyy/mm/dd.

4. Coseismic: 6 July 2017 M_w 6.5 Mainshock and M_w 5.8 Aftershock

The interseismic model of aseismic slip in Leyte suggests that the Tongonan section of the Philippine Fault could be locked. Following the 6 July 2017 M_w 6.5 earthquake in Leyte, we thus evaluate any potential overlap between seismic and aseismic slip. The M_w 6.5 event produced discontinuous surface ruptures, with quick-response surveys by PHIVOLCS (2017) indicating that slip was distributed along the known traces of the fault in Tongonan (Figure 11). Offset of concrete structures show around a maximum of 1.1 m of left-lateral displacement, with around 0.6 m vertical displacement (Llamas et al., 2017) (Figure 11b). The earthquake was followed by several aftershocks, the largest of which (a M_w 5.8 event) happened 4 days later on 10 July 2017, with a similar strike-slip mechanism (orange "beach ball" in Figure 11a). No historical earthquakes are known to have produced surface ruptures along this fault, although Besana and Ando (2005) suggest that earthquakes of magnitudes greater than 6.0 could have occurred in Leyte. More recently, Fukushima et al. (2019) highlight the similarity of the recorded waveforms of a M_s 6.9 event in 1947 and the 2017 mainshock.

The recent published slip models of the 6 July 2017 mainshock have used interferograms that span both the mainshock and the aftershock (Fukushima et al., 2019; Yang et al., 2018). Hence, these slip distributions actually show the combined seismic slip from the 6 July mainshock and the 10 July aftershock. As listed in Table 3, there is a Sentinel-1 acquisition one day after the mainshock. We therefore propose to constrain the deformation from the mainshock and aftershock independently. However, only one Sentinel-1 acquisition was realized between the two events, so information is available for only one line-of-sight in constraining the separate slip distributions of each event. ALOS-2, on the other hand, has only premainshock and postaftershock acquisitions, but data are available on both ascending and descending tracks. The modeling strategy we have developed to invert for the mainshock and aftershock slip distributions using all available interferograms (similar to Ragon et al., 2019) is described in the following section. This approach exploits the advantage of using different look geometries from distinct satellite tracks, providing more constraints to infer fault displacements.

4.1. Data and Methods

4.1.1. InSAR Data Processing

We used Sentinel-1 interferograms generated by the LiCSAR semiautomated processing chain (González et al., 2016). LiCSAR automatically combines bursts and subswaths of Sentinel-1 SLC images within predefined frames to create interferograms using GAMMA Software with minimal manual input. The interferograms were multilooked by 20 and 4 in azimuth and range, respectively, roughly equivalent to pixels of around 60 m × 60 m pixels. We took the unfiltered interferograms from LiCSAR frame 061D_07906_131313 (derived from Sentinel-1 descending Track 61 data) that covers Leyte. In the processing, we included the NAMRIA IfSAR DEM (the same as in section 3.1) for topographic corrections and geocoding.

The ALOS-2 interferograms, as in Fukushima et al. (2019), were processed using the RINC software (Ozawa et al., 2016) with the SRTM1 DEM for topographic phase and geocoding. These interferograms were multilooked to an equivalent pixel size of 100 m × 100 m in range and azimuth.

We used an adaptive spectral filter on both data sets to increase the signal-to-noise ratio (Goldstein & Werner, 1998, as described in section 3.1). We unwrapped each interferogram with a region-growing branch-cut algorithm (i.e., *grasses* program in GAMMA). In order to reduce the occurrence of unwrapping errors in the coseismic interferograms, we applied this method iteratively. We initially unwrapped regions with coherences above 0.8 and decreased the coherence threshold on each iteration. This step also flagged branch cuts to prevent unwrapping between pixels with sudden phase jumps, and then unwrapped small regions with high coherence. Succeeding iterations unwrapped areas with progressively lower coherence adjacent to the previously unwrapped regions. We manually checked for unwrapping errors at each iteration. Finally, from the result of the iteration with minimal unwrapping errors, we made manual corrections where necessary and masked any outstanding unwrapping errors that could not be corrected. For the Sentinel-1 interferograms, we did the filtering twice to make the unwrapping more efficient.

We estimated the noise covariance in each interferogram in regions where no coseismic deformation has been recorded, and downsampled the data for use in the inversion (both methods as described in section 3.4.3). The empirical standard deviation and correlation length of the Sentinel-1 coseismic data are ∼1.5 cm and ∼6 km, respectively. For the ALOS-2 data, these are ∼1 cm and 2 km, respectively. The covariance functions of the coseismic InSAR data sets can be found in supporting information Figure S10.

4.1.2. Inverting for Mainshock and Aftershock Slip

In order to obtain models of the mainshock and aftershock slip, we set up the inverse problem considering the different data sets (Table 3). The long temporal baseline of the ALOS-2 interferograms means that they include some interseismic (preseismic) and postseismic slip. For example, the premainshock acquisition of the ALOS-2 ascending Track 24 is almost 1.5 yr prior to the M_w 6.5 event, which means that there could be up to almost 6 cm of left-lateral displacement on sections that slip aseismically.

To separate the mainshock, aftershock, and preseismic and postseismic slips, we write the direct problem as

$$\overbrace{\begin{bmatrix} \mathbf{d}^{M}_{Sent1_{d1}} \\ \mathbf{d}^{A}_{Sent1_{d2}} \\ \mathbf{d}^{MA}_{Sent1_{d3}} \\ \mathbf{d}^{MA}_{ALOS2_{d}} \\ \mathbf{d}^{MA}_{ALOS2_{a}} \end{bmatrix}}^{\mathbf{d}} = \overbrace{\begin{bmatrix} \mathbf{G}^{M}_{Sent1_{d1}} & 0 & 0 \\ 0 & \mathbf{G}^{A}_{Sent1_{d2}} & 0 \\ \mathbf{G}^{M}_{Sent1_{d3}} & \mathbf{G}^{A}_{Sent1_{d3}} & 0 \\ \mathbf{G}^{M}_{ALOS2_{d}} & \mathbf{G}^{A}_{ALOS2_{d}} & \mathbf{G}^{P}_{ALOS2_{d}} \\ \mathbf{G}^{M}_{ALOS2_{a}} & \mathbf{G}^{A}_{ALOS2_{a}} & \mathbf{G}^{P}_{ALOS2_{a}} \end{bmatrix}}^{\mathbf{G}} \overbrace{\begin{bmatrix} \mathbf{m}^{M} \\ \mathbf{m}^{A} \\ \mathbf{m}^{P} \\ \\ \\ \end{bmatrix}}^{\mathbf{m}}. \tag{4}$$

On the left-hand side, the **d** vector contains the five LOS displacement observations including only one or both of the mainshock- and aftershock-related signals (superscripts M and A, respectively), along either the ascending (subscript a) or descending (d) LOS from the ALOS-2 and Sentinel-1 satellites. The **G** matrix is a combination of Green's functions that relate slip on the fault from different source patches of the fault (**m**) to the observations in **d**. $\mathbf{m}^M$ is the distribution of the mainshock coseismic slip, $\mathbf{m}^A$ is the distribution of the aftershock coseismic slip, and $\mathbf{m}^P$ is the distribution of the sum of preseismic and postseismic slip recorded by the ALOS-2 interferograms. We also include terms in **G** and **m** that allow us to fit a residual ramp for each individual data set.

We used the same fault parametrization of the Northern Leyte Segment as in the interseismic model (section 3.4.2), but use only the onshore patches. Our prior PDF is uniform for all strike-slip parameters, between −5 and 300 cm, and Gaussian for the dip-slip component (mean at 0 cm and the 3σ probability range within −200 and 200 cm). Positive values of slip indicate left-lateral and reverse slip for strike slip and dip-slip, respectively.

As we also modeled the coseismic slip with AlTar, we primarily cite, in the following sections, the mean and standard deviation of the posterior PDF of slip, unless otherwise stated. We find that the mean and the mode of the posterior PDF are not significantly different (comparisons can be found in supporting information Figure S11). The fit of the model prediction to the observations are shown in supporting information Figure S12 for the Sentinel-1 data, and supporting information Figure S13 for the ALOS-2 data.

4.2. Results: Surface Deformation and Slip on the Fault

The interferograms clearly show the left-lateral deformation related to the M_w 6.5 mainshock and the M_w 5.8 aftershock. As respectively displayed in Figure 12 and Figure 13c, descending track Sentinel-1 and ALOS-2 interferograms show movement away from satellite LOS east of the fault, and displacement in the opposite sense on the west side. This is apparent despite poor coherence in the Sentinel-1 data near the fault.

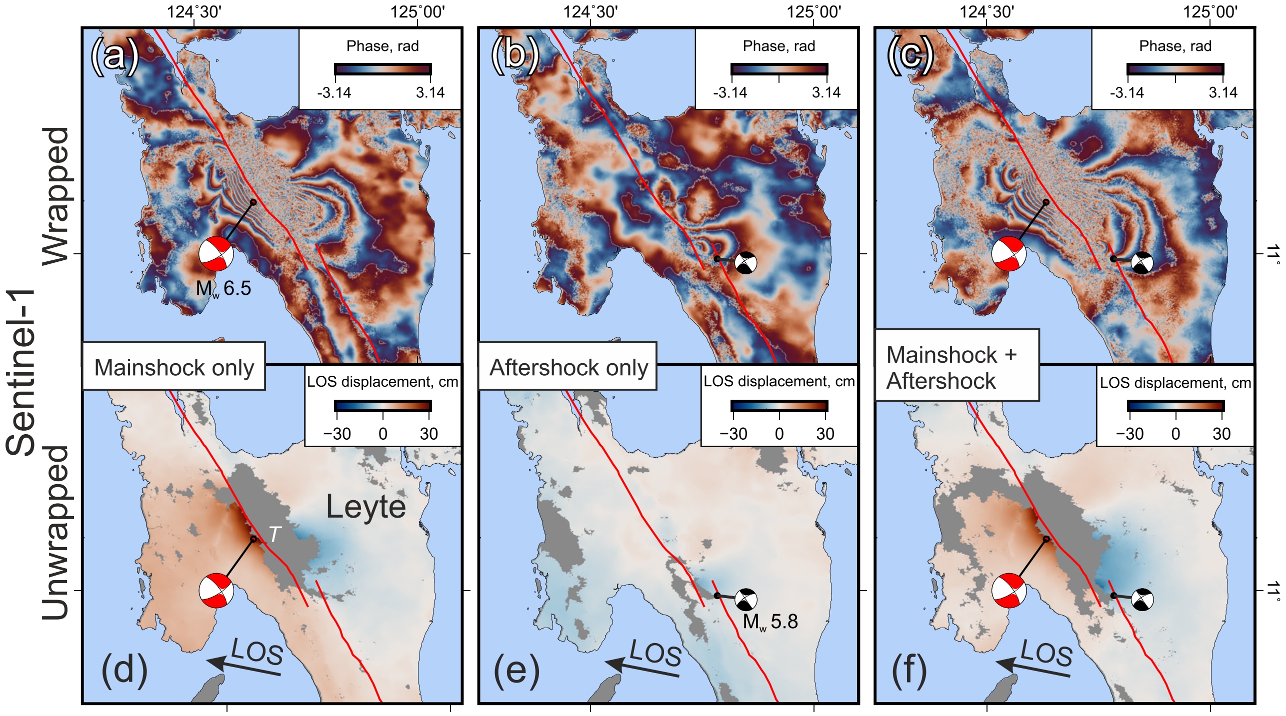

Figure 12. Pairs of wrapped and unwrapped coseismic interferograms, from Sentinel-1 data, showing phase change and line-of-sight (LOS) displacement of either the 6 July mainshock (M_w 6.5) or the 10 July aftershock (M_w 5.8), and their combined signal. Each map pair shows filtered wrapped interferogram (top) and unwrapped displacement (bottom). Positive unwrapped LOS displacement indicates movement toward the satellite. Focal mechanisms of the earthquakes are included for reference. T: Tongonan. (a, d) Sentinel-1 descending Track 61 data, showing mainshock displacement only. (b, e) Same track, but showing aftershock displacement only. (c, f) Combined mainshock and aftershock displacement from Sentinel-1 descending Track 61.

In the ascending track ALOS-2 interferogram (Figure 13d), we note an opposite sign of LOS displacement compared to that in the descending track interferogram (Figure 13c). Thanks to the good coherence to the west of the fault in all interferograms, we can observe large LOS displacement right along the Tongonan Segment of the fault (white T in Figure 12d). This coincides with the location of the largest reported surface displacements in the field (Llamas et al., 2017; PHIVOLCS, 2017).

Comparing the Sentinel-1 wrapped interferograms that include the mainshock and the aftershock separately (Figures 12a and 12b, respectively) reveals that most of the deformation occurring during the aftershock happened south of the mainshock. Discontinuities in the wrapped phase of both the mainshock and aftershock data appear to be on the same fault trace (the Tongonan Segment). For the aftershock, this discontinuity is just south of the fault bend. These observations strongly suggest that both seismic events ruptured the Tongonan Segment, but at different locations.

The model slip distributions in Figure 12 suggest that most of the seismic slip from both events occurred at depths shallower than 7 km. The largest magnitude of slip for the mainshock is confined within the upper 2 km of the fault, with up to 152 ± 21 cm of left-lateral slip (Figure 14a). This corresponds well with the location of the mapped surface ruptures in Tongonan (Figure 11a and 11b). The modeled strike-slip magnitude is only slightly higher than the observed field offsets (~1.1 m, PHIVOLCS, 2017) (Figure 11c). Likewise, vertical displacements can also be observed in the field, with the eastern side downthrown by about 50 cm (PHIVOLCS, 2017) (Figure 11b). In our model, dip-slip of 27 ± 33 cm on the patch with the greatest slip reflects this but is not as well constrained as the strike slip (i.e., the standard deviation is larger than the mean). The discrepancies between the field observations and the model may be due to local ground conditions that can attenuate slip, and may also reflect limitations imposed by the size of the model's shallowest patches.

The aftershock model shows slip on fault patches directly south of the mainshock deformation, with a maximum slip of 36 ± 10 cm at depths between 2 and 7 km (Figure 14b). As similarly apparent in the interferograms, it is notable that most of the aftershock slip is located just south of the fault bend. This may

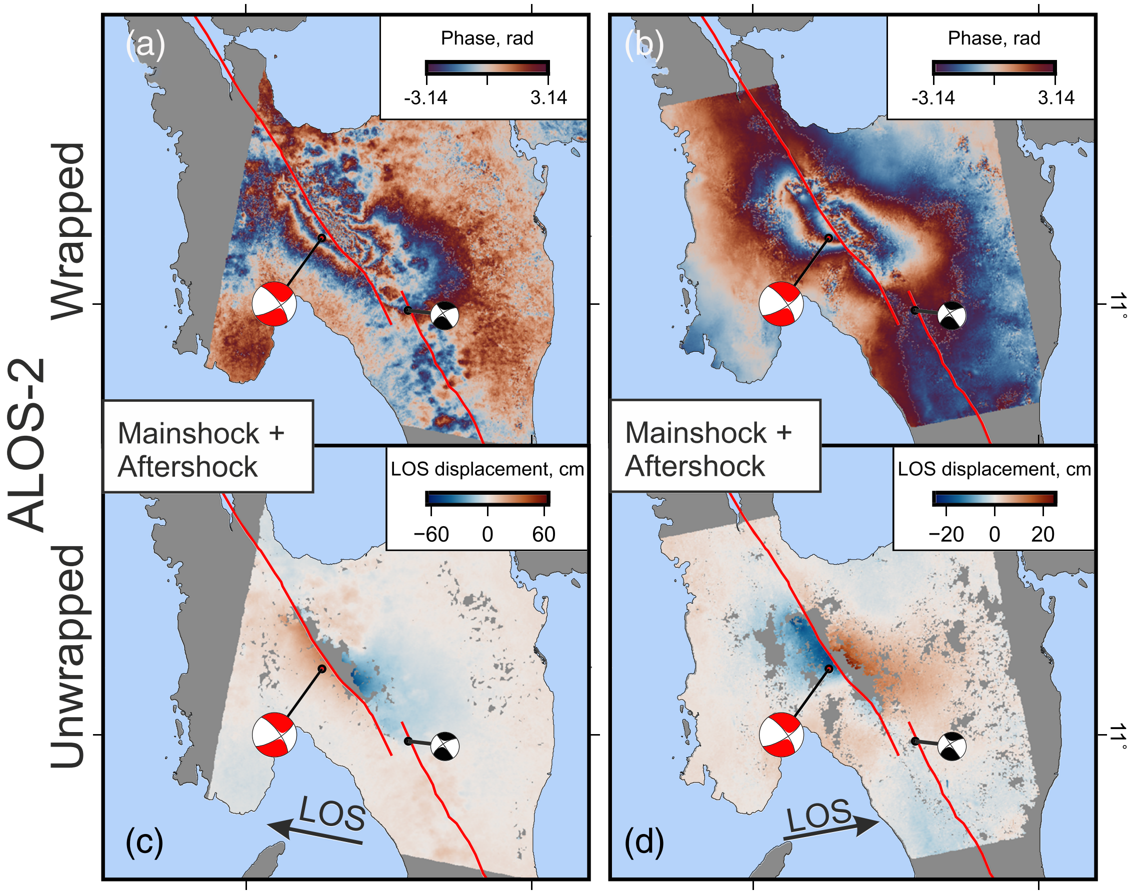

Figure 13. Pairs of wrapped and unwrapped coseismic interferograms, from ALOS-2 data, showing phase change and LOS displacement. These interferograms include both the 6 July mainshock (M_w 6.5) and the 10 July aftershock (M_w 5.8). Each map pair shows filtered wrapped interferogram (top) and unwrapped displacement (bottom). Positive unwrapped LOS displacement indicates movement toward the satellite. Focal mechanisms of the mainshock (red) and aftershock (black) are included for reference. ALOS-2 descending Track 136 (a, c), and ALOS-2 ascending Track 24 (b, d). See Table 3 for details of interferogram pairs.

indicate that the fault geometry played a role in the spatiotemporal distribution of seismic slip, which is an implication we discuss further in the discussion that follows. Comparing the distribution of total seismic slip with the aseismic slip model shows the coincidence of the seismic slip distribution with the patches that have a significant slip deficit in the interseismic period (Figure 14c).

5. Discussion

Different lines of evidence have been used to investigate the nature and causes of aseismic fault slip (see reviews by Avouac, 2015; Bürgmann, 2018; Harris, 2017). Our slip models representing different stages of the seismic cycle provide a basis for discussion of the mechanics of faulting, such as what controls seismic rupture extent and why faults slip aseismically, and earthquake recurrence. One important aspect of our modeling, which makes it reasonable to compare the slip distributions for different stages of the seismic cycle, is that we independently derived the interseismic and coseismic models with few a priori assumptions on the slip distribution or the relationship of the two modes of slip—our only assumption being the fixed fault geometry.

5.1. Complementary Distribution of Seismic and Aseismic Slip

Juxtaposing the extent of shallow seismic slip with the along-strike variations of interseismic slip rate, we can observe the clear complementarity between them (Figure 15). This is also apparent when comparing the interseismic and coseismic slip models (Figure 14c). If we consider a rate-and-state friction perspective, the retardation of seismic slip can be related to the frictional properties of a rate-strengthening (RS) material

(a) Mainshock

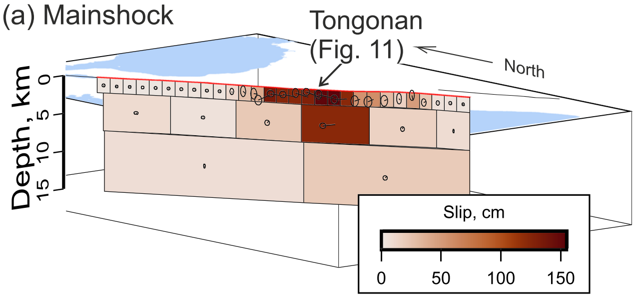

(b) Aftershock

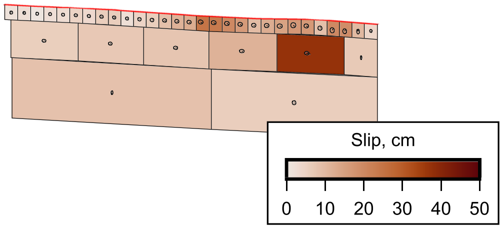

(c) Total seismic slip

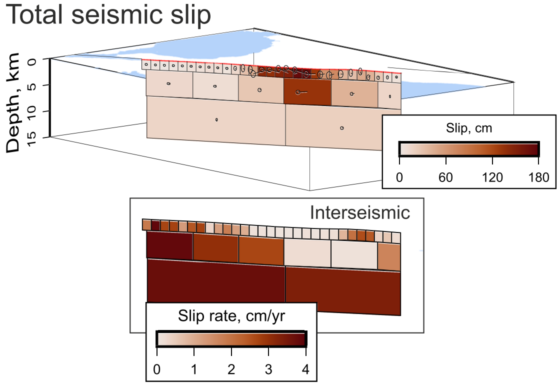

Figure 14. (a) Posterior mean slip model, in cm, for the 6 July 2017 M_w 6.5 mainshock. Arrows and ellipses show slip direction and 95% confidence interval, respectively. (b) The same, but for the 10 July 2017 M_w 5.8 aftershock. (c) Combined mainshock and aftershock slip. Inset: Interseismic aseismic slip distribution on the same segment (as in Figure 8).

(Scholz, 1998). The existence of such a material along the fault will have two impacts: (1) increase of friction with increasing rate of slip will slow and potentially arrest a rupture propagating at seismic rate and (2) a RS material favors aseismic slip during the interseismic period. The latter consequence reduces the shear stress available on the fault that could otherwise have helped the seismic rupture to propagate, even in a RS environment (Kaneko et al., 2010; Thomas, Lapusta, et al., 2014).

Figure 15 suggests that seismic slip did propagate slightly into the sections that slip aseismically by no more than 5 km to the north and 10 km to the south. As demonstrated by numerical models of fault slip, the stress changes ahead of the rupture tip can permit the coseismic rupture to propagate into RS zones (e.g., Boatwright & Cocco, 1996; Tse & Rice, 1986; Thomas, Lapusta, et al., 2014). The propagation of seismic slip into sections with low slip deficit may also be attributed to the partial coupling on patches that do not slip aseismically at the full tectonic rate, as this leads to stress accumulation as described above (Kaneko et al., 2010).

We note that our ability to resolve slip variability in Leyte is limited by the patch sizes of our discretized fault model, that is, we only have slip measurements every 2 km at the surface.

5.2. The Role of Geometry and Structural Complexity on Seismic and Aseismic Slip Distribution

Observations of the relationship between fault geometry and variations in aseismic slip rate are limited. Nevertheless, Moore and Byerlee (1992) suggest there is a link between the orientation of secondary

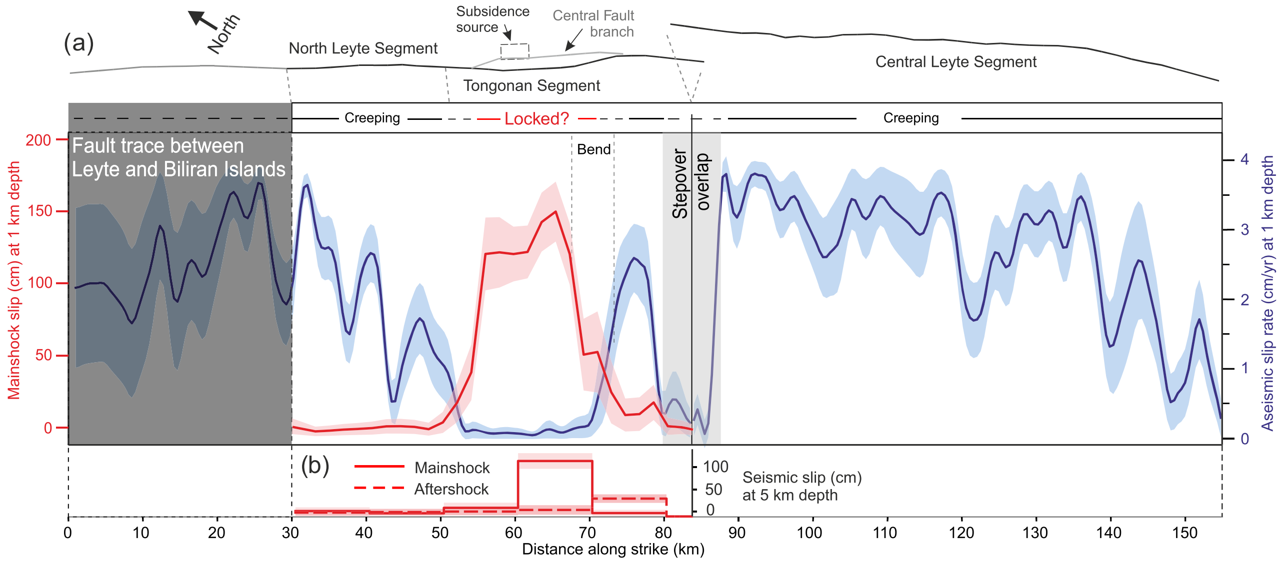

Figure 15. Rate and extent of aseismic and seismic slip on the Philippine Fault in Leyte. (a) Interseismic slip rate (blue) and strike-slip component of M_w 6.5 mainshock (red) at 1 km depth. Shaded area from 0–30 km distance indicates section of the fault that goes off the coast of Leyte, where slip at 1 km depth may be poorly resolved. Map view of the surface trace of the main Philippine Fault and Central Fault branch, and surface projection of the subsidence source is also shown for reference. Light blue and pink area: 1σ uncertainty range slip of aseismic and seismic slip, respectively. (b) Seismic slip at 5 km depth from the 6 July M_w 6.5 mainshock (red solid line) and the 10 July M_w 5.8 aftershock (dashed line), taken from slip of patches on the middle row of the models (Figure 14). Pink area also indicates 1σ uncertainty range.

structures (e.g., Riedel-type shears) and the sliding dynamics (seismic or aseismic behavior). Observations of aseismic slip on the Haiyuan Fault (China) show that bursts of slow slip are constrained by fault geometry (Jolivet, Candela, et al., 2015). Romanet et al. (2018) have also demonstrated numerically that a fault with parallel branches and no variations in frictional properties can influence the sliding dynamics. On the other hand, many studies have highlighted how fault bends and stepovers appear to control the extent of seismic ruptures (e.g., Biasi & Wesnousky, 2017; Wesnousky, 2006, and references therein).

In Leyte, the southern limit of the seismic slip distribution of the M_w 6.5 earthquake coincides with the fault bend, south of Tongonan. The Tongonan Segment ruptured further south of the bend during the M_w 5.8 aftershock, 4 days after the mainshock, at slightly greater depths than during the mainshock (Figures 14 and 15b). This suggests that, instead of rupturing the whole locked section in one event, the fault bend may have controlled the spatiotemporal distribution of seismic slip during the July 2017 earthquake sequence.

In terms of the interseismic slip distirbution, as we noted in section 3.5, residuals near Tongonan from our interseismic model might be related to the simplicity of the fault geometry used. If we consider faults from detailed maps of structures in the geothermal area, the linear trend in the data and residuals (Figures 8c and 8e) appears to coincide with the Central Fault Line subbranch. Detailed structural studies of the geothermal area (e.g., Aurelio et al., 1993; Caranto & Jara, 2015) also suggest that there are several other secondary faults in Tongonan, not considered in our model.

The presence of these off-main fault structures are consistent with what can be expected along intersegments (e.g., Manighetti et al., 2015; Perrin et al., 2016, and references therein). Thus, strain dissipation may occur across several structures while shallower patches on the main fault in Tongonan remain locked during the interseismic.

To explore the effects of a more complex fault geometry on our results, we perform a separate test with a model that includes a Central Fault branch. We discretize the Central Fault as a vertical strike-slip fault with 2-km-long patches that extend to 2 km depth from the surface, and assign broad uniform priors (−4 to 4 cm/yr). While this doesn't completely get rid of the residuals, the model resolves aseismic slip on the Central Fault (supporting information Figures S14 and S15, respectively), and the Tongonan Segment appears to remain locked. Including even more secondary faults, based on detailed structural maps, may provide more realistic models and would probably further improve the model predictions, but better data coverage would then be required (e.g., InSAR observations from different look angles with less decorrelation, dense continuous GPS coverage). Moreover, on a broad scale, large residuals in the near-fault zone are apparent only in Tongonan.

Further work may also be done by comparing the inversion results with a detailed cartography of the microstructure around the different fault segments (e.g., damage, lithology, and permeability), something beyond the scope of this study. A complementary investigation of the afterslip will is also needed to understand further the physical parameters that control the spatiotemporal extent of the aseismic and seismic segments, and how they interact with each other.

5.3. Physical Factors That Can Lead to Aseismic Slip

Based on the rich existing literature, several physical parameters, such as lithology, ambient temperatures, local pore pressure, and seismic history, can lead to aseismic slip on faults (e.g., Avouac, 2015; Bürgmann, 2018; Harris, 2017).

The active hydrothermal system in Leyte has been advocated as a factor promoting aseismic slip (Duquesnoy et al., 1994). The circulation of heated fluids causes significant mineral alteration in geothermal systems in the Philippines (Reyes, 1990), leading to deposits with RS phyllosilicates, as observed on other comparable structures, for example, the San Andreas Fault and the Longitudinal Valley Fault (Moore & Rymer, 2007; Thomas, Avouac, Gratier, & Lee, 2014, respectively). In Leyte, mineralogical and geochemical analyses of lithologies encountered in geothermal exploration wells in Tongonan show extensive phyllosilicate alteration in the subsurface, with assemblages including talc, chlorite, smectite, and illite (Reyes, 1990; Scott, 2001). Depending on the ambient temperatures, these minerals and rock formations can display a RS or a rate-weakening (RW) behavior (Blanpied et al., 1991; den Hartog et al., 2012; Okamoto et al., 2019; Scholz, 1998; Saffer & Marone, 2003). Temperatures in the geothermal wells in Tongonan at depths where these minerals are found range between 100°C and 300°C (Reyes, 1990; Scott, 2001). Furthermore, exploration wells drilled into the Quaternary volcanoes in central Leyte show that the volcanic deposits are generally andesitic, and that the underlying Leyte ultramafic basement is as shallow as 800–1,600 m depth (Ramos & Rigor, 2005). They report that these basement rocks are serpentinized—with secondary minerals like talc, chlorite, actinolite, and antigorite—and have poor permeability for geothermal resource interests. As noted in section 2.2, serpentinites, particularly those bearing talc, have been correlated to aseismic slip on creeping sections of the San Andreas Fault (Moore & Rymer, 2007). Related laboratory experiments further tested how the shearing of serpentinites against quartz-bearing rocks promotes aseismic slip (Moore & Lockner, 2013). The shallow occurrence of serpentinized rocks across Leyte (e.g., Cole et al., 1989; Suerte et al., 2005; as shown in Figure 2a) alongside young andesitic volcanism could thus explain the inferred aseismic slip in our model at depth.

The presence of fluids can also favor pressure solution creep as observed along the Parkfield segment (Gratier et al., 2011) and on the Longitudinal Valley Fault (Thomas, Avouac, Gratier, & Lee, 2014). In central Leyte, fluid upflow through the impermeable basement from depth is believed to be restricted to existing structural channels like andesitic dikes and faults (Ramos & Rigor, 2005). Besides, fluids can induce elevated pore pressure conditions on the fault, thus reducing effective normal stress, which, if maintained for a long time, will further aseismic slip.

That being said, the above suggestions make it difficult to explain why the Tongonan Segment is locked, despite its location near the largest geothermal power plant of the Philippines, where extensive alteration and higher pore pressures from the abundant amount of geothermal fluids can be expected. Geothermal resource surveys have indicated that the Tongonan Segment has poor permeability and low resource potential (Caranto & Jara, 2015). In that case, fluid circulation, and therefore mineral alteration and/or pressure solution can be limited, thus favoring a RW type of behavior. In addition, one cannot exclude possible along-strike variations of lithology. The potential influence of the net fluid loss from geothermal production on the stress field also needs to be carefully considered. If the removal of fluids from the geothermal reservoir causes fluid-saturated faults to drain (lowering pore pressure), then normal stress on the fault will increase. This may be the case for the shallowest faults close to the subsidence source. However, whether anthropogenic activity in the upper 2 km can affect the stresses at deeper patches (i.e., greater than 2 km depth) or not is an open question, given that we can expect natural circulation of hydrothermal fluids across the volcanic arc. Detailed analysis of fault zone lithology and geophysical data will be needed before we can directly correlate the myriad of conditions in Leyte with the behavior of the fault.

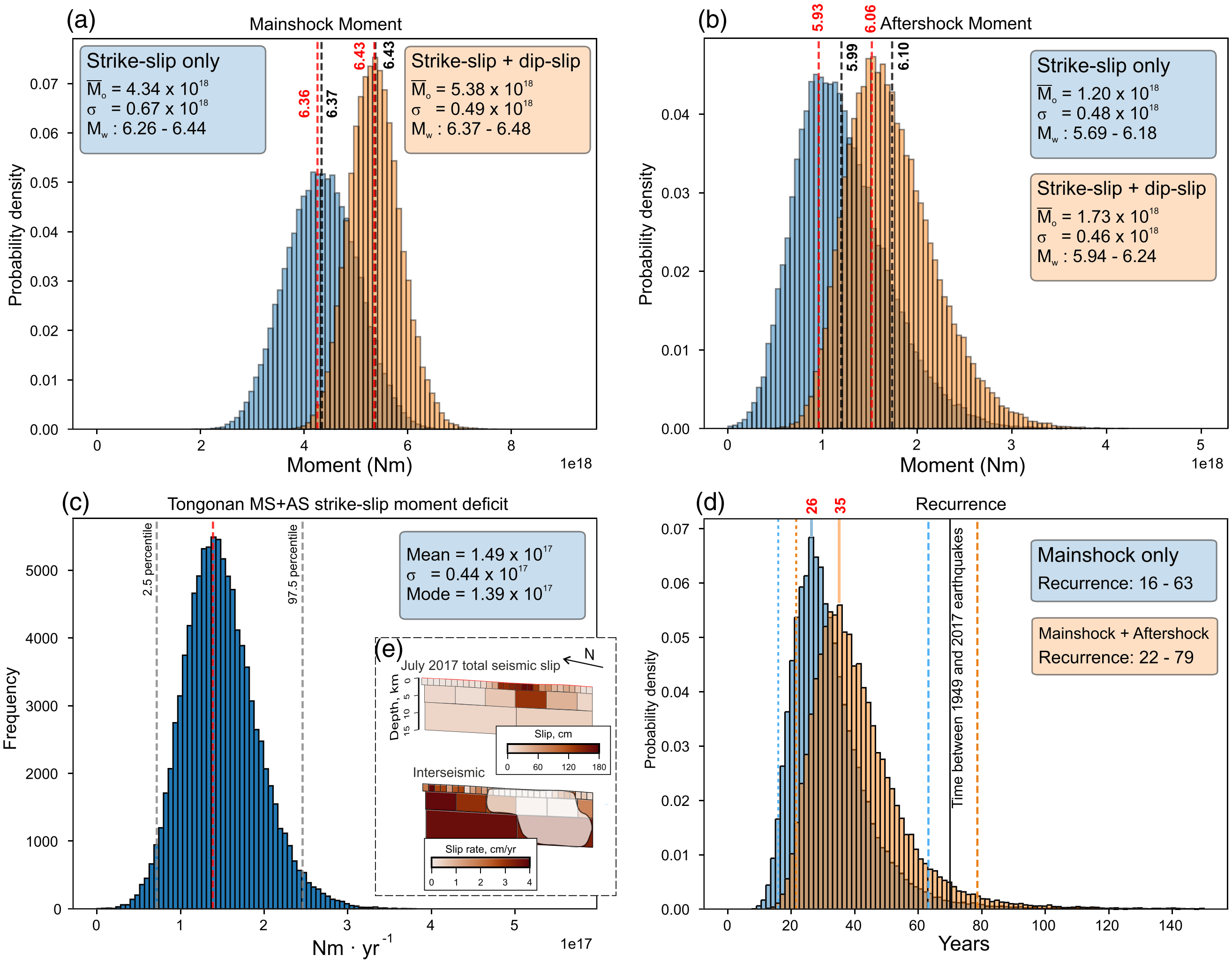

Figure 16. Probability distribution of seismic and aseismic slip budget, and return period. (a) Seismic moment of 6 July 2017 mainshock. Blue PDF corresponds to the seismic moment if we include only the strike-slip component. Orange PDF shows the seismic moment when we include both strike-slip and dip-slip components. Red and black dashed lines indicate the mode and the mean of the PDF, respectively, labeled with the equivalent moment magnitude. (b) The same as (a) but for the 10 July 2017 aftershock. (c) Interseismic strike-slip moment deficit rate. Interval between dotted and dashed lines indicates the 95% confidence interval. (d) Return period PDF for events similar to the mainshock only (blue) and combined moment of the mainshock and the aftershock (orange). Recurrence range is based on the lower and upper bounds of the return period 95% confidence interval. (e) Coseismic and interseismic models, with white shaded area showing patches used in the slip budget calculation.

5.4. Seismic and Aseismic Slip Budget: Probabilistic Return Period of Significant Earthquakes on the Tongonan Segment

Our modeling results allow the estimation of the relative proportion of coseismic and interseismic slip on the Leyte segment of the Philippine Fault, and, thus, permit us to draw inferences regarding the return period of earthquakes in this area. It is important to note the large uncertainties involved in this discussion, as all possible sources of errors, arising from measurement errors and modeling assumptions, are difficult to fully follow through. Furthermore, we can only compare the coseismic strike-slip component with our interseismic model, as the latter does not include dip-slip. However, it is still worth illustrating the kind of questions that can be addressed based on the probabilistic modeling presented in this paper.

From our ensemble of probable coseismic slip models, we can draw a probability distribution of seismic moment (M_o) (e.g., Minson et al., 2014). As shown in Figure 16, if we consider only the patches below Tongonan, the mainshock moment follows a Gaussian distribution with a mean of 4.34×10^{18} N m (~M_w 6.4) and a standard deviation of 0.67×10^{18} N m (hereafter referred to as $4.34 \pm 0.67 \times 10^{18}$ N m). Equivalently, the aftershock moment is $1.20 \pm 0.48 \times 10^{18}$ N m (~M_w 5.9). The seismic moments reported by the USGS for

Table 4
Seismic Moment (M_o) *and Moment Magnitude* (M_w) *Estimates of the July 2017 Earthquakes*

	Seismic moment (10^{18} Nm), and magnitude				
	Seismological	Geodetic			
		This study			
	USGS	Strike slip only[a]	SS + DS[b]	F2019[c]	Y2018[d]
Mainshock	7.06 (M_w 6.5)	4.34 ± 0.67 (M_w 6.3–6.4)	5.38 ± 0.49 (M_w 6.4–6.5)	6.80 (M_w 6.5)	7.78 (M_w 6.6)
Aftershock	0.721 (M_w 5.8)	1.20 ± 0.48 (M_w 5.7–6.2)	1.73 ± 0.46 (M_w 5.9–6.2)	—	—

Note. M_o uncertainties and M_w ranges are based on the standard deviation and the 2.5th and 97.5th percentiles of the marginals, respectively.
[a] Seismic moment obtained from strike-slip component only. [b] Seismic moment from total slip (combined strike-slip and dip-slip component). [c] From Fukushima et al. (2019), using only ALOS-2 data. [d] From Yang et al. (2018), using both Sentinel-1 and ALOS-2 data spanning both the mainshock and aftershock.

the mainshock and the aftershock are higher and lower, respectively, though the moment magnitudes do not differ greatly (Table 4). Our moment magnitude estimates for the mainshock are slightly smaller than the magnitudes from existing slip models also derived from InSAR data (Fukushima et al., 2019; Yang et al., 2018, Table 4). However, as previously mentioned in section 4, it is important to note that the interferograms used in these studies span the 10 July aftershock deformation as well. Discrepancies may also exist due to different fault parameterizations (e.g., Yang et al., 2018 and Fukushima et al., 2019 both suggest steep east dipping faults) and assumptions on the shear modulus of the fault, which for our estimates we set to 30 GPa. If we include the dip-slip component, the moment magnitude we obtain for both the mainshock and aftershock are only slightly higher (Table 4).

We can then compare the seismic moment of the July 2017 earthquakes with the slip deficit accumulated during interseismic period. Interseismic strain may translate to an accumulation of seismic moment deficit at a certain rate ($\dot{M}_{o_{deficit}}$). Similar to calculations of interseismic fault coupling (e.g., Mccaffrey, 2002), this can be computed by integrating the slip rate deficit over the locked fault area (the slip potency deficit; e.g., Thomas, Avouac, Champenois, et al., 2014) and assuming a shear modulus (μ), as

$$\dot{M}_{o_{deficit}} = \mu \sum_i \left(V_{LG} - V_{int_i} \right) A_i, \tag{5}$$

where A_i is the area of the fault patch, V_{LG} is the long-term slip rate, and V_{int_i} is the slip rate during the interseismic period. Obtaining a PDF of $\dot{M}_{o_{deficit}}$ from our posterior PDF of interseismic slip (e.g., Michel et al., 2017) suggests that seismic moment deficit accumulates at a rate of $1.49 \pm 0.44 \times 10^{17}$ N m/yr (~M_w 5.4 per year) along the Tongonan Segment (Figure 16c), assuming that our model of interseismic slip deeper than 15 km depth (3.3 ± 0.2 cm/yr) is representative of V_{LG}.

The return period (T) of earthquakes like the July 2017 events can be estimated, given that

$$T = \frac{M_{o_{July2017}}}{\dot{M}_{o_{deficit}}}. \tag{6}$$

Through random sampling of the interseismic slip rate and coseismic slip probability distributions, we obtain a probability distribution for the return period. In Tongonan, events with the same seismic moment as the mainshock can have a return period of any span between 16 and 63 yr (based on the 95% confidence interval of the PDF; blue distribution in Figure 16d). For the combined moment of the mainshock and aftershock strike slip ($5.54 \pm 0.57 \times 10^{18}$ N m), the likely return period range becomes 22–79 yr (orange PDF in Figure 16d). The 70-year interval between the June 1947 M_s 6.9 and July 2017 M_w 6.5 earthquakes is at the upper end of the tail of the PDF for the mainshock only return period, while it is within the 2σ bounds of the PDF for the combined mainshock-aftershock case (orange PDF in Figure 16d). In principle, accurate assessments of earthquake recurrence should also include the cumulative moment released during the afterslip period, which we have not isolated in this study. If the Philippine Fault in Leyte behaves similarly to the Longitudinal Valley Fault after the M_w 6.8 2003 Chengkung earthquake, this is not a negligible amount (e.g., 75% of the coseismic moment; Thomas, Avouac, Champenois, et al., 2014). Therefore, including afterslip in the calculation could significantly increase the return period of M_w 6.5 earthquakes in the area (shifting our return period PDFs to higher values).

Smaller aftershocks would only slightly increase the return period (i.e., the next largest ones, other than the aftershock we model, are mb 5.0 and mb 5.3 events that may increase the return period PDF by a few years), and we also do not account for the possibility of off-fault earthquakes.

Finally, we note that, while we have assumed a value for the shear modulus to determine the equivalent interseismic moment deficit and coseismic moment, Equation 6 shows that our estimates of the return period are independent of the value of the shear modulus.

The aforementioned considerations, along with the complementarity of the aseismic and seismic slip distributions from our models (Figures 7 and 12), and the similarity of the waveforms of the 1947 and 2017 earthquakes (Fukushima et al., 2019), support the possibility that the Tongonan Segment may indeed be a site of repeating earthquakes with M_w about 6.5.

The seismic catalog of smaller earthquakes may warrant a closer look. If we were to compare the modern instrumental record (Figure 2) with the slip deficit and locking on the fault (Figure 15), there is a stark difference in the clustering of $M_s > 1$ seismicity between the partially locked Northern Leyte Segment and the generally uncoupled Central Leyte Segment. However, the location of the epicenters don't exactly plot directly on the main fault trace. Event relocation (e.g., Waldhauser & Ellsworth, 2000, among others) will be needed for a robust analysis to distinguish earthquakes that might be related to diffuse faulting in the vicinity of the relay zone from possible smaller asperities on the fault (Tse et al., 1985).

5.5. Limitations of Assuming Elastic Homogeneity

Our models and the correlation of the slip modes with different local geological features has led us to several physical explanations for the observed behavior of the Philippine Fault in Leyte. Nonetheless, the homogeneous elastic modeling approach, useful in understanding fault behavior to first order, has limitations in representing possible structural complexity. Microstructural studies suggest that well-developed fault damage zones can modify the elastic properties of the material surrounding the fault compared to background values (Faulkner et al., 2006; Walsh, 1965a, 1965b), resulting in lower S wave and P wave velocities in the damage zone (e.g., Froment et al., 2014). These lower values of the elastic moduli will have an impact on the amount of energy stored in the medium during the interseismic period. Furthermore, using a stratified elastic structure generally requires higher slip values near the surface to match geodetic observations (Jolivet, Simons, et al., 2015). Careful evaluation of the 3-D elastic structure is therefore needed here to further evaluate the effect of elastic heterogeneities on the distribution of seismic and aseismic slip, and therefore on the the return period of large earthquakes in the area.

6. Summary and Conclusions

We present the first probabilistic models of aseismic and coseismic slip along the Philippine Fault, specifically on Leyte island where the fault was generally thought of as aseismic prior to the earthquakes in July 2017. We highlight the spatial variations of aseismic slip rate along-strike and at depth, on around 100 km of the fault, with certain sections of the fault slipping aseismically at rates that match the long-term slip rate. We also identify the 20-km-long Tongonan Segment that accumulates significant slip deficit. This segment may represent a locked asperity that can be the site of recurring earthquakes, similar to the M_w 6.5 and M_w 5.8 earthquakes in July 2017. In this paper, we have drawn observations from geothermal exploration work—primarily, the presence of hydrothermal fluids and rate-strengthening minerals—that can explain the propensity of the Philippine Fault in Leyte to slip aseismically. Detailed mapping and laboratory analysis, however, are required to draw any steady conclusions especially when considering that part of the fault appears to be locked and seismogenic.

The role played by the complex fault architecture—like the bend, parallel branches, and secondary faults in Tongonan—needs to be investigated using better surface deformation data, along with a more detailed analysis of the reported low permeability on the Tongonan segment (Caranto & Jara, 2015). The coincidence of these factors could influence the slip dynamics and stressing rate on the locked fault patches (e.g., Ghosh et al., 1992; Romanet et al., 2018). This has implications for the estimation of earthquake recurrence, and, more generally, to our understanding of the factors that drive aseismic and seismic slip on faults.

More broadly, in the regional tectonic sense, the July 2017 earthquakes in Leyte fall within the ideas of slip decoupling and strain partitioning across the Philippine Mobile Belt (Aurelio, 2000; Barrier et al., 1991;

Fitch, 1972; McCaffrey, 1996). Our models provide a detailed look on the heterogeneity of the mode of deformation on the Philippine Fault and provides new insights to the active tectonics of the Philippines.

Appendix A: Estimating Step Change on Profiles

To estimate the magnitude of the step in the line-of-sight profiles, we fit a LOS velocity model, v, with the functional form (modified from Pousse Beltran et al., 2016, see also Larson et al., 2004)

$$v(x) = v_0 + \frac{u}{2}\left[\tanh\left(\frac{x - x_0}{d}\right) - 1\right], \tag{A1}$$

to each profile, where x is the distance from the fault, v_0 is the far-field velocity on the profile, u is the step in velocity, x_0 is the horizontal position of the step, and d is the horizontal length scale of the step. We only estimate a step on profiles that have a distinct difference in the surface velocity across the fault.

Appendix B: Resolution Analysis

The resolving power of inversions can be described by a resolution matrix, **R** (e.g., Atzori & Antonioli, 2011; Funning et al., 2005; Jackson, 1979; Sagiya & Thatcher, 1999, among many others), a diagonal matrix with values between 0 and 1 (inclusive). A resolution of 1 indicates fully resolved slip, while the resolution will be 0 if slip is unresolved. In probabilistic inversions, **R** can be formulated as

$$\mathbf{R} = \mathbf{C_m}\mathbf{G}^T(\mathbf{G}\mathbf{C_m}\mathbf{G}^T + \mathbf{C}_d)^{-1}\mathbf{G}, \tag{B1}$$

where C_m is a diagonal matrix that contains the standard deviation of the prior PDF of each slip parameter, and C_d is the data covariance matrix (Gombert et al., 2018; Jolivet et al., 2012; Tarantola, 2005). The resolution matrix essentially gives us an idea of the ability of the data to constrain the slip on the individual patches (e.g., Loveless & Meade, 2011; Sagiya & Thatcher, 1999).

Data Availability Statement

The ALOS data set for the interseismic period is ©JAXA, METI and includes data accessed through ASF DAAC (https://www.asf.alaska.edu). Sentinel-1 coseismic interferograms contain modified Copernicus Sentinel data (2017), freely available at https://scihub.copernicus.eu/, with LiCSAR data processing done using CEDA/JASMIN cluster facilities. ALOS-2 interferograms are from the PALSAR-2 data shared among the PALSAR Interferometry Consortium to Study our Evolving Land Surface (PIXEL). These data were provided by the Japan Aerospace Exploration Agency (JAXA) under a cooperative research contract with the Earthquake Research Institute of the University of Tokyo. The 5-m resolution DEM of Leyte island is courtesy of the National Mapping and Resource Information Agency (NAMRIA), Philippines. Generic Mapping Tools (Wessel et al., 2013) and Scientific Color Maps (http://www.fabiocrameri.ch/colourmaps.php Crameri, 2019) were used to prepare figures.

Acknowledgments

We would like to thank the Editor and two anonymous reviewers for their comments that helped improve the manuscript. We thank the European Space Agency (ESA) and COMET for the quick response to the request for additional acquisition of Sentinel-1 data right after the 6 July 2017 earthquake. COMET is the Natural Environment Research Council (NERC) Centre for the Observation and Modelling of Earthquakes, Volcanoes and Tectonics, a partnership between UK Universities and the British Geological Survey. We also would like to acknowledge the support provided by the local government units of the Province of Leyte, the City of Ormoc, and the municipalities of Burauen, Abuyog, and Leyte in the conduct of field work. J. D. B. D. is supported by a PhD program grant, ID number 261465226, under the Newton Agham partnership. The grant is funded by the UK Department for Business, Energy and Industrial Strategy and the Philippines' Commission on Higher Education and delivered by the British Council. This work was also supported by funding from NERC through the Looking into the Continents from Space (LiCS) large grant (NE/K011006/1). This project has also received funding from the European Research Council (ERC) under the European Union's Horizon 2020 research and innovation program under grant agreement 758210 (Geo4D project).

References

Agram, P., Jolivet, R., Riel, B., Lin, Y., Simons, M., Hetland, E., & Lasserre, C.(2013). New Radar Interferometric Time Series Analysis Toolbox Released. *EOS Transactions*, *94*(7), 69–76. https://doi.org/10.1029/2011JB008731

Allen, C. R. (1962). Circum-Pacific faulting in the Philippines-Taiwan region. *Journal of Geophysical Research*, *67*(12), 4795–4812. https://doi.org/10.1029/JZ067i012p04795

Anderlini, L., Serpelloni, E., & Belardinelli, M. E. (2016). Creep and locking of a low-angle normal fault: Insights from the Altotiberina fault in the northern Apennines (Italy). *Geophysical Research Letters*, *43*, 4321–4329. https://doi.org/10.1002/2016GL068604

Apuada, N. A., Olivar, R. E. R., & Salonga, N. D. (2005). Repeat microgravity and leveling surveys at Leyte Geothermal Production Field, North Central Leyte, Philippines, *Proceedings of the Thirtieth Workshop on Geothermal Reservoir Engineering* (Vol. 30, pp. 403–411). Stanford, California: Stanford University, Stanford Geothermal Program.

Atzori, S., & Antonioli, A. (2011). Optimal fault resolution in geodetic inversion of coseismic data. *Geophysical Journal International*, *185*(1), 529–538. https://doi.org/10.1111/j.1365-246X.2011.04955.x

Aurelio, M. A. (2000). Shear partitioning in the Philippines: Contraints from the Philippine fault and global positioning system data. *Island Arc*, *9*(4), 584–597. https://doi.org/10.1046/j.1440-1738.2000.00304.x

Aurelio, M. A., Pagado, E. S., & Tebar, H. J. (1993). Kinematics of Philippine Fault system at the Tongonan Geothermal Field, N. Leyte: Implications for geothermal exploration and development. *Journal of the Geological Society of the Philippines*, *48*(1–2), 1–20.

Aurelio, M. A., Peña, R. E., & Taguibao, K. J. L. (2013). Sculpting the Philippine archipelago since the Cretaceous through rifting, oceanic spreading, subduction, obduction, collision and strike-slip faulting: Contribution to IGMA5000. *Journal of Asian Earth Sciences*, *72*, 102–107. https://doi.org/10.1016/j.jseaes.2012.10.007

Avouac, J. P. (2015). From geodetic imaging of seismic and aseismic fault slip to dynamic modeling of the seismic cycle. *Annual Review of Earth and Planetary Sciences*, *43*(1), 150223150959000. https://doi.org/10.1146/annurev-earth-060614-105302

Bürgmann, R. (2018). The geophysics, geology and mechanics of slow fault slip. *Earth and Planetary Science Letters*, *495*, 112–134. https://doi.org/10.1016/j.epsl.2018.04.062

Bacolcol, T., Barrier, E., Duquesnoy, T., Aguilar, A., Jorgio, R., de la Cruz, R., & Lasala, M. (2005). GPS Constraints on Philippine Fault slip rate in Masbate Island, central Philippines. *Journal of the Geological Society of the Philippines*, *60*(1–2), 1–7.

Bagnardi, M., & Hooper, A. (2018). Inversion of surface deformation data for rapid estimates of source parameters and uncertainties: A Bayesian approach. *Geochemistry, Geophysics, Geosystems*, *19*, 2194–2211. https://doi.org/10.1029/2018GC007585

Bakun, W. H., Aagaard, B., Dost, B., Ellsworth, W. L., Hardebeck, J. L., Harris, R. A., & Waldhauser, F. (2005). Implications for prediction and hazard assessment from the 2004 Parkfield earthquake. *Nature*, *437*(7061), 969–974. https://doi.org/10.1038/nature04067

Barrier, E., Huchon, P., & Aurelio, M. A. (1991). Philippine Fault: A key for Philippine kinematics. *Geology*, *19*(1), 32–35. https://doi.org/10.1130/0091-7613(1991)019<0032:PFAKFP>2.3.CO;2

Bautista, M. L. P., & Oike, K. (2000). Estimation of the magnitudes and epicenters of Philippine historical earthquakes. *Tectonophysics*, *317*, 137–169. https://doi.org/10.1016/S0040-1951(99)00272-3

Besana, G. M., & Ando, M. (2005). The central Philippine Fault Zone: Location of great earthquakes, slow events, and creep activity. *Earth, Planets and Space*, *57*(10), 987–994. https://doi.org/10.1186/BF03351877

Biasi, G. P., & Wesnousky, S. G. (2017). Bends and ends of surface ruptures. *Bulletin of the Seismological Society of America*, *107*, 2543–2560. https://doi.org/10.1785/0120160292

Blanpied, M., Lockner, D., & Byerlee, D. (1991). Fault stability at hydrothermal conditions. *Geophysical Research Letters*, *18*(4), 609–612.

Boatwright, J., & Cocco, M. (1996). Frictional constraints on crustal faulting. *Journal of Geophysical Research*, *101*, 13,895–13,909. https://doi.org/10.1029/96JB00405

Burgmann, R., Schmidt, D., Nadeau, R. M., D'Alessio, M., Fielding, E., Manaker, D., & Murray, M. H. (2000). Earthquake potential along the northern Hayward Fault, California. *Science*, *289*(5482), 1178–1182. https://doi.org/10.1126/science.289.5482.1178

Caranto, J. A., & Jara, M. P. (2015). Factors controlling reservoir permeability at the Leyte Geothermal Production Field, Tongonan, Philippines. In *Proceedings: World Geothermal Congress 2015*. Melbourne, Australia.

Cavalié, O., Lasserre, C., Doin, M. P., Peltzer, G., Sun, J., Xu, X., & Shen, Z. K. (2008). Measurement of interseismic strain across the Haiyuan fault (Gansu, China), by InSAR. *Earth and Planetary Science Letters*, *275*(3–4), 246–257. https://doi.org/10.1016/j.epsl.2008.07.057

Cetin, E., Cakir, Z., Meghraoui, M., Ergintav, S., & Akoglu, A. M. (2014). Extent and distribution of aseismic slip on the Ismetpaa segment of the North Anatolian Fault (Turkey) from Persistent Scatterer InSAR. *Geochemistry, Geophysics, Geosystems*, *15*, 2883–2894. https://doi.org/10.1002/2014GC005307

Chaussard, E., Bürgmann, R., Fattahi, H., Johnson, C. W., Nadeau, R., Taira, T., & Johanson, I. (2015). Interseismic coupling and refined earthquake potential on the Hayward-Calaveras fault zone. *Journal of Geophysical Research: Solid Earth*, *120*, 8570–8590. https://doi.org/10.1002/2015JB012230

Cole, J., McCabe, R., Moriarty, T., Malicse, J. A., Delfin, F. G., Tebar, H., & Ferrer, H. P. (1989). A preliminary Neogene paleomagnetic data set from Leyte and its relation to motion on the Philippine fault. *Tectonophysics*, *168*(1–3), 205–220. https://doi.org/10.1016/0040-1951(89)90376-4

Crameri, F. (2019). Scientific colour maps. https://zenodo.org/record/3596401

DeMets, C., Gordon, R. G., & Argus, D. F. (2010). Geologically current plate motions. *Geophysical Journal International*, *181*(1), 1–80. https://doi.org/10.1111/j.1365-246X.2009.04491.x

den Hartog, S. A., Niemeijer, A. R., & Spiers, C. J. (2012). New constraints on megathrust slip stability under subduction zone *P-T* conditions. *Earth and Planetary Science Letters*, *353-354*, 240–252. https://doi.org/10.1016/j.epsl.2012.08.022

Deng, J. (1998). Viscoelastic flow in the lower crust after the 1992 Landers, California, earthquake. *Science*, *282*(5394), 1689–1692. https://doi.org/10.1126/science.282.5394.1689

Dimalanta, C. B., Suerte, L. O., Yumul, G. P., Tamayo, R. A., & Ramos, E. G. L. (2006). A Cretaceous supra-subduction oceanic basin source for Central Philippine ophiolitic basement complexes: Geological and geophysical constraints. *Geosciences Journal*, *10*(3), 305–320. https://doi.org/10.1007/BF02910372

Doin, M. P., Lodge, F., Guillaso, S., Jolivet, R., Lasserre, C., Ducret, G., & Pinel, V. (2011). Presentation of the small baseline NSBAS processing chain on a case example: The Etna deformation monitoring from 2003 to 2010 using Envisat data. In *Proceedings: ESA Fringe 2011 Workshop*. ESA, Frascati, Italy.

Duputel, Z., Jiang, J., Jolivet, R., Simons, M., Rivera, L., Ampuero, J. P., & Minson, S. E. (2015). The Iquique earthquake sequence of April 2014: Bayesian modeling accounting for prediction uncertainty. *Geophysical Research Letters*, *42*, 7949–7957. https://doi.org/10.1002/2015GL065402

Duquesnoy, T. (1997). Contribution de la géodésie à l'étude de grands décrochements actifs associés à des zones de subduction à convergence oblique Exemples de la grande faille de Sumatra et de la faille Philippine (Unpublished doctoral dissertation). Univ. Paris-Sud, Orsay, France.

Duquesnoy, T., Barrier, E., Kasser, M., Aurelio, M., Gaulon, R., Punongbayan, R. S., & Rangin, C.(1994). Detection of creep along the Philippine Fault: First results of geodetic measurements on Leyte Island, central Philippine. *Geophysical Research Letters*, *21*(11), 975–978. https://doi.org/10.1029/94GL00640

Elliott, J. R., Walters, R. J., & Wright, T. J. (2016). The role of space-based observation in understanding and responding to active tectonics and earthquakes. *Nature Communications*, *7*, 1–16. https://doi.org/10.1038/ncomms13844

Fattahi, H., & Amelung, F. (2016). InSAR observations of strain accumulation and fault creep along the Chaman Fault system, Pakistan and Afghanistan. *Geophysical Research Letters*, *43*, 8399–8406. https://doi.org/10.1002/2016GL070121

Faulkner, D. R., Mitchell, T. M., Healy, D., & Heap, M. J. (2006). Slip on 'weak' faults by the rotation of regional stress in the fracture damage zone. *Nature*, *444*(7121), 922–925. https://doi.org/10.1038/nature05353

Fialko, Y., Simons, M., & Agnew, D. (2001). The complete (3-D) surface displacement field in the epicentral area of the 1999 Mw7.1 Hector Mine earthquake, California, from space geodetic observations. *Geophysical Research Letters*, *28*(16), 3063–3066.

Fitch, T. J. (1972). Plate convergence, transcurrent faults, and internal deformation adjacent to Southeast Asia and the Western Pacific. *Journal of Geophysical Research*, *77*(23), 4432–4460.

Froment, B., McGuire, J. J., van Hilst, R. D., Gouédard, P., Roland, E. C., Zhang, H., & Collins, J. A. (2014). Imaging along-strike variations in mechanical properties of the Gofar transform fault, East Pacific Rise. *Journal of Geophysical Research: Solid Earth*, *119*, 7175–7194. https://doi.org/10.1002/2014JB011270.Received

Fukushima, Y., Hashimoto, M., Miyazawa, M., Uchida, N., & Taira, T. (2019). Surface creep rate distribution along the Philippine fault, Leyte Island, and possible repeating of Mw ∼6.5 earthquakes on an isolated locked patch. *Earth, Planets and Space*, *71*(118), 22. https://doi.org/10.1186/s40623-019-1096-5

Funning, G. J., Parsons, B., Wright, T. J., Jackson, J. A., & Fielding, E. J. (2005). Surface displacements and source parameters of the 2003 Bam (Iran) earthquake from Envisat advanced synthetic aperture radar imagery. *Journal of Geophysical Research*, *110*, 1–23. https://doi.org/10.1029/2004JB003338

GRASS Development Team (2017). Geographic Resources Analysis Support System (GRASS GIS) Software, Version 7.2. https://grass.osgeo.org

Galgana, G., Hamburger, M., McCaffrey, R., Corpuz, E., & Chen, Q. (2007). Analysis of crustal deformation in Luzon, Philippines using geodetic observations and earthquake focal mechanisms. *Tectonophysics*, *432*(1–4), 63–87. https://doi.org/10.1016/j.tecto.2006.12.001

Ghosh, U., Mukhopadhyay, A., & Sen, S. (1992). On two interacting creeping vertical surface-breaking strike-slip faults in a two-layer model of the lithosphere. *Physics of the Earth and Planetary Interiors*, *70*(1–2), 119–129. https://doi.org/10.1016/0031-9201(92)90166-S

Goldstein, R. M., & Werner, C. L. (1998). Radar interferogram filtering for geophysical applications. *Geophysical Research Letters*, *25*(21), 4035–4038. https://doi.org/10.1029/1998GL900033

Gomba, G., Parizzi, A., De Zan, F., Eineder, M., & Bamler, R. (2016). Toward operational compensation of ionospheric effects in SAR interferograms: The split-spectrum method. *IEEE Transactions on Geoscience and Remote Sensing*, *54*(3), 1446–1461. https://doi.org/10.1109/TGRS.2015.2481079

Gombert, B., Duputel, Z., Jolivet, R., Doubre, C., Rivera, L., & Simons, M. (2018). Revisiting the 1992 Landers earthquake: A Bayesian exploration of co-seismic slip and off-fault damage. *Geophysical Journal International*, *212*, 839–852. https://doi.org/10.1093/gji/ggx455

González, P., Walters, R., Hatton, E., Spaans, K., McDougall, A., Hooper, A., & Wright, T. (2016). LiCSAR: Tools for automated generation of Sentinel-1 frame interferograms. Paper presented at AGU Fall Meeting 2016, San Francisco, CA, USA.

Gratier, J. P., Richard, J., Renard, F., Mittempergher, S., Doan, M. L., Di Toro, G., & Boullier, A. M. (2011). Aseismic sliding of active faults by pressure solution creep: Evidence from the San Andreas fault observatory at Depth. *Geology*, *39*(12), 1131–1134. https://doi.org/10.1130/G32073.1

Guotana, J. M., Payot, B. D., Dimalanta, C. B., Ramos, N. T., Faustino-Eslava, D. V., Queaño, K. L., & Yumul, G. P. (2018). Petrological and geochemical characteristics of the Samar Ophiolite ultramafic section: Implications on the origins of the ophiolites in Samar and Leyte islands, Philippines. *International Geology Review*, *60*(4), 401–417. https://doi.org/10.1080/00206814.2017.1336944

Harris, R. A. (2017). Large earthquakes and creeping faults. *Reviews of Geophysics*, *55*, 169–198. https://doi.org/10.1002/2016RG000539

Hazel, M., Uribe, C., Dacillo, D. B., Dacoag, L. M., Andrino, R. P., & Alcober, E. H. (2015). 30 years of Tongonan-1 (Leyte, Philippines) sustained production. In *Proceedings: World Geothermal Congress 2015*. Melbourne, Australia.

Hsu, Y. J., Yu, S. B., Loveless, J. P., Bacolcol, T., Solidum, R., Luis, A., & Woessner, J. (2016). Interseismic deformation and moment deficit along the Manila subduction zone and the Philippine Fault system. *Journal of Geophysical Research: Solid Earth*, *121*, 7639–7665. https://doi.org/10.1002/2016JB013082

Jackson, D. D. (1979). The use of a priori data to resolve non-uniqueness in linear inversion. *Geophysical Journal of the Royal Astronomical Society*, *57*(1), 137–157. https://doi.org/10.1111/j.1365-246X.1979.tb03777.x

Johnson, K. M. (2013). Is stress accumulating on the creeping section of the San Andreas fault? *Geophysical Research Letters*, *40*, 6101–6105. https://doi.org/10.1002/2013GL058184

Jolivet, R., Agram, P. S., Lin, N. Y., Simons, M., Doin, M. P., Peltzer, G., & Li, Z. (2014). Improving InSAR geodesy using global atmospheric models. *Journal of Geophysical Research: Solid Earth*, *119*, 2324–2341. https://doi.org/10.1002/2013JB010588

Jolivet, R., Candela, T., Lasserre, C., Renard, F., Klinger, Y., & Doin, M. P. (2015). The burst-like behavior of aseismic slip on a rough fault: The creeping section of the Haiyuan fault, China. *Bulletin of the Seismological Society of America*, *105*(1), 480–488. https://doi.org/10.1785/0120140237

Jolivet, R., & Frank, W. B. (2020). The transient and intermittent nature of slow slip. *AGU Advances*, *1*, e2019AV000126. https://doi.org/10.1029/2019AV000126

Jolivet, R., Lasserre, C., Doin, M. P., Guillaso, S., Peltzer, G., Dailu, R., & Xu, X. (2012). Shallow creep on the Haiyuan fault (Gansu, China) revealed by SAR interferometry. *Journal of Geophysical Research*, *117*, B06401. https://doi.org/10.1029/2011JB008732

Jolivet, R., Lasserre, C., Doin, M. P., Peltzer, G., Avouac, J. P., Sun, J., & Dailu, R. (2013). Spatio-temporal evolution of aseismic slip along the Haiyuan fault, China: Implications for fault frictional properties. *Earth and Planetary Science Letters*, *377-378*, 23–33. https://doi.org/10.1016/j.epsl.2013.07.020

Jolivet, R., Simons, M., Agram, P. S., Duputel, Z., & Shen, Z. (2015). Aseismic slip and seismogenic coupling along the central San Andreas Fault. *Geophysical Research Letters*, *42*, 297–306. https://doi.org/10.1002/2014GL062222

Kaneko, Y., Avouac, J. P., & Lapusta, N. (2010). Towards inferring earthquake patterns from geodetic observations of interseismic coupling. *Nature Geoscience*, *3*(5), 363–369. https://doi.org/10.1038/ngeo843

Lagmay, A. M. F. A., Tengonciang, A. M. P., Marcos, H. V., & Pascua, C. S. (2003). A structural model guide for geothermal exploration in Ancestral Mount Bao, Leyte, Philippines. *Journal of Volcanology and Geothermal Research*, *122*(1–2), 133–141. https://doi.org/10.1016/S0377-0273(02)00501-2

Larson, K. M., Lowry, A. R., Kostoglodov, V., Hutton, W., Sánchez, O., Hudnut, K., & Suárez, G. (2004). Crustal deformation measurements in Guerrero, Mexico. *Journal of Geophysical Research*, *109*, B04409. https://doi.org/10.1029/2003JB002843

Lienkaemper, J. J., McFarland, F. S., Simpson, R. W., Bilham, R. G., Ponce, D. A., Boatwright, J. J., & John Caskey, S. (2012). Long-term creep rates on the Hayward Fault: Evidence for controls on the size and frequency of large earthquakes. *Bulletin of the Seismological Society of America*, *102*(1), 31–41. https://doi.org/10.1785/0120110033

Lindsey, E. O., Fialko, Y., Bock, Y., Sandwell, D. T., & Bilham, R. (2014). Localized and distributed creep along the southern San Andreas Fault. *Journal of Geophysical Research: Solid Earth*, *119*, 7909–7922. https://doi.org/10.1002/2014JB011275.1

Llamas, D. C., Marfito, B., Pogay, C., Vitto, K., Mangahas, R., Cahulogan, M., & Perez, J. (2017). Surface rupture associated with the 2017 magnitude 6.5 Leyte earthquake. *Paper presented at the Geological Society of the Philippines Convention 2017*. Makati, Philippines.

Lohman, R. B., & Simons, M. (2005). Some thoughts on the use of InSAR data to constrain models of surface deformation: Noise structure and data downsampling. *Geochemistry, Geophysics, Geosystems*, *6*, Q01007. https://doi.org/10.1029/2004GC000841

Loveless, J. P., & Meade, B. J. (2011). Spatial correlation of interseismic coupling and coseismic rupture extent of the 2011 $M_W = 9.0$ Tohoku-oki earthquake. *Geophysical Research Letters*, *38*, L17306. https://doi.org/10.1029/2011GL048561

Luzon, P. K., Montalbo, K., Galang, J., Sabado, J. M., Escape, C. M., Felix, R., & Lagmay, A. M. F. (2016). Hazard mapping related to structurally controlled landslides in Southern Leyte, Philippines. *Natural Hazards and Earth System Sciences*, *16*(3), 875–883. https://doi.org/10.5194/nhess-16-875-2016

Manighetti, I., Caulet, C., Barros, L. D., Perrin, C., Cappa, F., & Gaudemer, Y. (2015). Generic along-strike segmentation of Afar normal faults, East Africa: Implications on fault growth and stress heterogeneity on seismogenic fault planes. *Geochemistry, Geophysics, Geosystems*, *16*, 443–467. https://doi.org/10.1002/2014GC005691

Massonnet, D., Rossi, M., Carmona, C., Adragna, F., Peltzer, G., Felgl, K., & Rabaute, T. (1993). The displacement field of the Landers earthquake mapped by radar interferometry. *Nature*, *364*, 138–142.

McCaffrey, R. (1996). Slip partitioning at convergent plate boundaries of SE Asia. *Geological Society Special Publication*, *106*, 3–18. https://doi.org/10.1144/GSL.SP.1996.106.01.02

Mccaffrey, R. (2002). Crustal block rotations and plate coupling. In S. Stein, & J. Freynuekker (Eds.), *Plate boundary zones, Geodynamic Series 30* (pp. 101–122). Washington DC: American Geophysical Union. https://doi.org/10.1029/gd030p0101

Michel, S., Avouac, J., Jolivet, R., & Wang, L. (2017). Seismic and aseismic moment budget and implication for the seismic potential of the Parkfield segment of the San Andreas Fault. *Bulletin of the Seismological Society of America*, *108*(1), 19–38. https://doi.org/10.1785/0120160290

Minson, S. E., Simons, M., & Beck, J. L. (2013). Bayesian inversion for finite fault earthquake source models I—Theory and algorithm. *Geophysical Journal International*, *194*(3), 1701–1726. https://doi.org/10.1093/gji/ggt180

Minson, S. E., Simons, M., Beck, J. L., Ortega, F., Jiang, J., Owen, S. E., & Sladen, A. (2014). Bayesian inversion for finite fault earthquake source models—II: The 2011 great Tohoku-oki, Japan earthquake. *Geophysical Journal International*, *198*(2), 922–940. https://doi.org/10.1093/gji/ggu170

Moore, D. E., & Byerlee, J. (1992). Relationships between sliding behavior and internal geometry of laboratory fault zones and some creeping and locked strike-slip faults of California. *Tectonophysics*, *211*(1–4), 305–316. https://doi.org/10.1016/0040-1951(92)90067-G

Moore, D. E., & Lockner, D. A. (2013). Chemical controls on fault behavior: Weakening of serpentinite sheared against quartz-bearing rocks and its significance for fault creep in the San Andreas system. *Journal of Geophysical Research: Solid Earth*, *118*, 2558–2570. https://doi.org/10.1002/jgrb.50140

Moore, D. E., & Rymer, M. J. (2007). Talc-bearing serpentinite and the creeping section of the San Andreas fault. *Nature*, *448*(7155), 795–797. https://doi.org/10.1038/nature06064

Noda, H., & Lapusta, N. (2013). Stable creeping fault segments can become destructive as a result of dynamic weakening. *Nature*, *493*, 7433. https://doi.org/10.1038/nature11703

Okada, Y. (1985). Surface deformation due to shear and tensile faults in a half-space. *Bulletin Seismological Society of America*, *75*(4), 1135–1154.

Okamoto, A. S., Verberne, B. A., Niemeijer, A. R., Takahashi, M., Shimizu, I., Ueda, T., & Spiers, C. J. (2019). Frictional properties of simulated chlorite gouge at hydrothermal conditions: Implications for subduction megathrusts. *Journal of Geophysical Research: Solid Earth*, *124*, 4545–4565. https://doi.org/10.1029/2018JB017205

Ozawa, T., Fujita, E., & Ueda, H. (2016). Crustal deformation associated with the 2016 Kumamoto earthquake and its effect on the magma system of Aso volcano. *Earth, Planets and Space*, *68*(1), 186. https://doi.org/10.1186/s40623-016-0563-5

PHIVOLCS (2016). Distribution of active faults and trenches in the Philippines.

PHIVOLCS (2017). The 06 July 2017 magnitude 6.5 earthquake in Leyte. https://www.phivolcs.dost.gov.ph/index.php/news/638-poster-of-the-06-july-2017-magnitude-6-5-earthquake-in-leyte-2

PHIVOLCS (2018). 10 February 2017 Ms 6.7 Surigao del Norte earthquake: PHIVOLCS special report. Quezon City, Philippines, DOST-PHIVOLCS.

Peltzer, G., Crampé, F., Hensley, S., & Rosen, P. (2001). Transient strain accumulation and fault interaction in the Eastern California shear zone. *Geology*, *29*(11), 975–978. https://doi.org/10.1130/0091-7613(2001)029<0975:TSAAFI>2.0.CO;2

Perez, J. S., & Tsutsumi, H. (2017). Tectonic geomorphology and paleoseismology of the Surigao segment of the Philippine fault in northeastern Mindanao Island, Philippines. *Tectonophysics*, *699*, 244–257. https://doi.org/10.1016/j.tecto.2017.02.001

Perrin, C., Manighetti, I., Ampuero, J. P., Cappa, F., & Gaudemer, Y. (2016). Location of largest earthquake slip and fast rupture controlled by along-strike change in fault structural maturity due to fault growth. *Journal of Geophysical Research: Solid Earth*, *121*, 3666–3685. https://doi.org/10.1002/2015JB012671

Pousse Beltran, L., Pathier, E., Jouanne, F., Vassallo, R., Reinoza, C., Audemard, F., & Volat, M. (2016). Spatial and temporal variations in creep rate along the El Pilar fault at the Caribbean-South American plate boundary (Venezuela), from InSAR. *Journal of Geophysical Research: Solid Earth*, *121*, 8276–8296. https://doi.org/10.1002/2016JB013121

Price, E. J., & Sandwell, D. T. (1998). Small-scale deformations associated with the 1992 Landers, California, earthquake mapped by synthetic aperture radar interferometry phase gradients. *Journal of Geophysical Research*, *103*(B11), 27,001–27,016. https://doi.org/10.1029/98JB01821

Prioul, R., Cornet, F. H., Dorbath, C., Dorbath, L., Ogena, M., & Ramos, E. (2000). An induced seismicity experiment across a creeping segment of the Philippine Fault. *Journal of Geophysical Research*, *105*(B6), 13,595–13,612. https://doi.org/10.1029/2000JB900052

Punongbayan, R. S., Rimando, R. E., Daligdig, J. A., Besana, G. M., Daag, A. S., Nakata, T., & Tsutsumi, H. (1992). The 16 July 1990 Luzon earthquake ground rupture. The July 16, 1990 Luzon earthquake: A technical monograph, 1–32.

Ragon, T., Sladen, A., Bletery, Q., Vergnolle, M., Cavalié, O., Avallone, A., & Delouis, B. (2019). Joint inversion of coseismic and early postseismic slip to optimize the information content in geodetic data: Application to the 2009 Mw6.3 L'Aquila Earthquake, Central Italy. *Journal of Geophysical Research: Solid Earth*, *124*, 10,522–10,543. https://doi.org/10.1029/2018JB017053

Ramos, S. G., & Rigor, D. M. (2005). Lobi and Mahagnao: Geothermal prospects in an ultramafic setting central Leyte, Philippines. In *Proceedings: World Geothermal Congress 2005*, Antalya, Turkey.

Receveur, M., Sigmundsson, F., Drouin, V., & Parks, M. (2019). Ground deformation due to steam cap processes at Reykjanes, SW-Iceland: Effects of geothermal exploitation inferred from interferometric analysis of Sentinel-1 images 2015–2017. *Geophysical Journal International*, *216*(3), 2183–2212. https://doi.org/10.1093/gji/ggy540

Reyes, A. G. (1990). Petrology of Philippine geothermal systems and the application of alteration mineralogy to their assessment. *Journal of Volcanology and Geothermal Research*, *43*(1–4), 279–309. https://doi.org/10.1016/0377-0273(90)90057-M

Romanet, P., Bhat, H. S., Jolivet, R., & Madariaga, R. (2018). Fast and slow slip events emerge due to fault geometrical complexity. *Geophysical Research Letters*, *45*, 4809–4819. https://doi.org/10.1029/2018GL077579

Saffer, D. M., & Marone, C. (2003). Comparison of smectite- and illite-rich gouge frictional properties: Application to the updip limit of the seismogenic zone along subduction megathrusts. *Earth and Planetary Science Letters*, *215*(1–2), 219–235. https://doi.org/10.1016/S0012-821X(03)00424-2

Sagiya, T., & Thatcher, W. (1999). Coseismic slip resolution along a plate boundary megathrust: The Nankai Trough, southwest Japan. *Journal of Geophysical Research*, *104*(B1), 1111–1129. https://doi.org/10.1029/98JB02644

Sandwell, D. T., Myer, D., Mellors, R., Shimada, M., Brooks, B., & Foster, J. (2008). Accuracy and resolution of ALOS interferometry: Vector deformation maps of the Father's Day intrusion at Kilauea. *IEEE Transactions on Geoscience and Remote Sensing*, *46*(11), 3524–3534. https://doi.org/10.1109/TGRS.2008.2000634

Savage, J. C., & Burford, R. O. (1973). Geodetic determination of relative plate motion in central California. *Journal of Geophysical Research*, *78*(5), 832–845.

Scholz, C. H. (1998). Earthquakes and friction laws. *Nature*, *391*(6662), 37–42. https://doi.org/10.1038/34097

Scott, G. L. (2001). Hydrothermal alteration and fluid geochemistry of the Tongonan Geothermal Field, Philippines. *Resource Geology*, *51*(2), 117–134. https://doi.org/10.1111/j.1751-3928.2001.tb00086.x

Silcock, D. M., & Beavan, J. (2001). Geodetic constraints on coseismic rupture during the 1990 Ms 7.8 Luzon, Philippines, earthquake. *Geochemistry, Geophysics, Geosystems*, *2*(7), 1016. https://doi.org/10.1029/2000GC000101

Storchak, D. A., Harris, J., Brown, L., Lieser, K., Shumba, B., Verney, R., & Korger, E. I. (2017). Rebuild of the Bulletin of the International Seismological Centre (ISC), Part 1: 1964–1979. *Geoscience Letters*, *4*, 1. https://doi.org/10.1186/s40562-017-0098-z

Sudhaus, H., & Jónsson, S. (2009). Improved source modelling through combined use of InSAR and GPS under consideration of correlated data errors: Application to the June 2000 Kleifarvatn earthquake, Iceland. *Geophysical Journal International*, *176*(2), 389–404. https://doi.org/10.1111/j.1365-246X.2008.03989.x

Suerte, L. O., Yumul, G. P., Tamayo, R. A., Dimalanta, C. B., Zhou, M. F., Maury, R. C., & Balce, C. L. (2005). Geology, geochemistry and U-Pb SHRIMP age of the Tacloban Ophiolite Complex, Leyte Island (Central Philippines): Implications for the existence and extent of the proto-Philippine Sea Plate. *Resource Geology*, *55*(3), 207–216. https://doi.org/10.1111/j.1751-3928.2005.tb00242.x

Tarantola, A. (2005). Inverse problem theory and methods for model parameter estimation.

Thomas, M. Y., Avouac, J. P., Champenois, J., Lee, J. C., & Kuo, L. C. (2014). Spatiotemporal evolution of seismic and aseismic slip on the Longitudinal Valley Fault, Taiwan. *Journal of Geophysical Research: Solid Earth*, *119*, 5114–5139. https://doi.org/10.1002/2013JB010603

Thomas, M. Y., Avouac, J. P., Gratier, J. P., & Lee, J. C. (2014). Lithological control on the deformation mechanism and the mode of fault slip on the Longitudinal Valley Fault, Taiwan. *Tectonophysics*, *632*(C), 48–63. https://doi.org/10.1016/j.tecto.2014.05.038

Thomas, M. Y., Avouac, J. P., & Lapusta, N. (2017). Rate-and-state friction properties of the Longitudinal Valley Fault from kinematic and dynamic modeling of seismic and aseismic slip. *Journal of Geophysical Research: Solid Earth*, *122*, 3115–3137. https://doi.org/10.1002/2016JB013615

Thomas, M. Y., Lapusta, N., Noda, H., & Avouac, J. P. (2014). Quasi-dynamic versus fully dynamic simulations of earthquakes and aseismic slip with and without enhanced coseismic weakening. *Journal of Geophysical Research: Solid Earth*, *119*, 1986–2004. https://doi.org/10.1002/2013JB010615

Tong, X., Sandwell, D. T., & Schmidt, D. A. (2018). Surface creep rate and moment accumulation rate along the Aceh segment of the Sumatran Fault from L-band ALOS-1/PALSAR-1 observations. *Geophysical Research Letters*, *45*(8), 3404–3412. https://doi.org/10.1002/2017GL076723

Tse, S. T., Dmowska, R., & Rice, J. R. (1985). Stressing of locked patches along a creeping fault. *Bulletin of the Seismological Society of America*, *75*(3), 709–736.

Tse, S. T., & Rice, J. R. (1986). Crustal earthquake instability in relation to the depth variation of frictional slip properties. *Journal of Geophysical Research*, *91*(B9), 9452. https://doi.org/10.1029/jb091ib09p09452

Tsutsumi, H., & Perez, J. S. (2013). Large-scale active fault map of The Philippines based on aerial photograph interpretation. *Active Fault Research*, *39*(39), 29–37.

Tsutsumi, H., Perez, J. S., & Lienkaemper, J. J. (2016). Variation of surface creep rate along the Philippine Fault based on surveys of alinement arrays and offset cultural features. Paper presented at the American Geophysical Union Fall Meeting 2016, T23A–2907.

Tsutsumi, H., Perez, J. S., Marjes, J. U., Papiona, K. L., & Ramos, N. T. (2015). Coseismic displacement and recurrence interval of the 1973 Ragay Gulf earthquake, Southern Luzon, Philippines. *Journal of Disaster Research*, *10*(1), 83–90.

Tymofyeyeva, E., & Fialko, Y. (2018). Geodetic evidence for a blind fault segment at the southern end of the San Jacinto Fault Zone. *Journal of Geophysical Research: Solid Earth*, *123*, 878–891. https://doi.org/10.1002/2017JB014477

Waldhauser, F., & Ellsworth, W. L. (2000). A double-difference earthquake location algorithm: Method and application to the northern Hayward Fault, California. *Bulletin of the Seismological Society of America*, *90*(6), 1353–1368. https://doi.org/10.1785/0120000006

Walsh, J. B. (1965a). The effect of cracks in rocks on Poisson's ratio. *Journal of Geophysical Research*, *70*(20), 5249–5257. https://doi.org/10.1029/jz070i020p05249

Walsh, J. B. (1965b). The effect of cracks on the compressibility of rock. *Journal of Geophysical Research*, *70*(2), 381–389. https://doi.org/10.1029/JB083iB09p04459

Werner, C., Wegmüller, U., Strozzi, T., & Wiesmann, A. (2002). Processing strategies for phase unwrapping for INSAR applications. In *Proceedings: European Conference on Synthetic Aperture Radar (EUSAR) 2002*, *1*, pp. 353–356.

Wesnousky, S. G. (2006). Predicting the endpoints of earthquake rupture. *Nature*, *444*, 358–360.

Wessel, P., Smith, W. H., Scharroo, R., Luis, J., & Wobbe, F. (2013). Generic mapping tools: Improved version released. *Eos*, *94*(45), 409–410. https://doi.org/10.1002/2013EO450001

Willis, B. (1944). Philippine earthquakes and structure. *Bulletin of the Seismological Society of America*, *34*(2), 69–81. https://doi.org/10.2307/1779766

Wright, T. J., Lu, Z., & Wicks, C. (2004). Constraining the slip distribution and fault geometry of the Mw 7.9, 3 November 2002, Denali fault earthquake with Interferometric Synthetic Aperture Radar and Global Positioning System data. *Bulletin of the Seismological Society of America*, *94*(6 SUPPL. B), 175–189. https://doi.org/10.1785/0120040623

Wright, T., Parsons, B., & Fielding, E. (2001). Measurement of interseismic strain accumulation the North Anatolian Fault by satellite radar interferometry. *Geophysical Research Letters*, *28*(10), 2117–2120. https://doi.org/10.1029/2000GL012850

Yang, Y., Tsai, M., Hu, J., Aurelio, M. A., Hashimoto, M., Escudero, J. A. P., & Chen, Q. (2018). Coseismic slip deficit of the 2017 Mw 6.5 Ormoc Earthquake that occurred along a creeping segment and geothermal field of the Philippine Fault. *Geophysical Research Letters*, *45*, 2659–2668. https://doi.org/10.1002/2017GL076417

Yu, S. B., Hsu, Y. J., Bacolcol, T., Yang, C. C., Tsai, Y. C., & Solidum, R. (2013). Present-day crustal deformation along the Philippine Fault in Luzon, Philippines. *Journal of Asian Earth Sciences*, *65*, 64–74. https://doi.org/10.1016/j.jseaes.2010.12.007